



HAL
open science

Persistent Sodium Current Drives Excitability of Immature Renshaw Cells in Early Embryonic Spinal Networks

Juliette Boeri, Hervé Le Corrond, François-Xavier Lejeune, Barbara Le Bras, Christine Mouffle, Monara Kaelle S.C. Angelim, Jean-Marie Mangin, Pascal Branchereau, Pascal Legendre, Antony Czarnecki

► **To cite this version:**

Juliette Boeri, Hervé Le Corrond, François-Xavier Lejeune, Barbara Le Bras, Christine Mouffle, et al.. Persistent Sodium Current Drives Excitability of Immature Renshaw Cells in Early Embryonic Spinal Networks. *Journal of Neuroscience*, 2018, 38 (35), pp.7667-7682. 10.1523/JNEUROSCI.3203-17.2018 . hal-03220695v2

HAL Id: hal-03220695

<https://hal.sorbonne-universite.fr/hal-03220695v2>

Submitted on 7 May 2021

HAL is a multi-disciplinary open access archive for the deposit and dissemination of scientific research documents, whether they are published or not. The documents may come from teaching and research institutions in France or abroad, or from public or private research centers.

L'archive ouverte pluridisciplinaire **HAL**, est destinée au dépôt et à la diffusion de documents scientifiques de niveau recherche, publiés ou non, émanant des établissements d'enseignement et de recherche français ou étrangers, des laboratoires publics ou privés.

Research Articles: Systems/Circuits

Persistent sodium current drives excitability of immature Renshaw cells in early embryonic spinal networks

Juliette Boeri^a, Hervé Le Corronc^{a,b}, François Xavier Lejeune^a, Barbara Le Bras^a, Christine Mouffle^a, Monara Kaelle S.C. Angelim^a, Jean Marie Mangin^a, Pascal Branchereau^{c,d}, Pascal Legendre^a and Antony Czarnecki^a

^aINSERM, UMR_S 1130, CNRS, UMR 8246, Neuroscience Paris Seine, Institute of Biology Paris Seine, 75005 Paris, France. Sorbonne Univ, UPMC Univ Paris 06, UM CR18, 75005 Paris, France.

^bUniv Angers, 49000 Angers, France.

^cBordeaux, INCIA, UMR 5287, F-33615 Pessac, France.

^dCNRS, INCIA, UMR 5287, F-33615 Pessac, France.

DOI: 10.1523/JNEUROSCI.3203-17.2018

Received: 8 November 2017

Revised: 14 June 2018

Accepted: 29 June 2018

Published: 16 July 2018

Author contributions: J.B., H.L.C., F.-X.L., B.L.B., M.K.S.A., P.B., P.L.nd A.C. performed research; J.B., H.L.C., F.-X.L., J.M.M., P.B., P.L.nd A.C. analyzed data; J.B., H.L.C., J.M.M., P.B., P.L.nd A.C. wrote the paper; H.L.C., P.B., P.L.nd A.C. designed research; C.M. contributed unpublished reagents/analytic tools.

Conflict of Interest: The authors declare no competing financial interests.

We thank Elim Hong for helpful discussion. This work was supported by FRM grant DEQ20160334891, AFM Grant 18564, the Institut National de la Santé et de la Recherche Médicale and the Centre National de la Recherche Scientifique. The authors declare no competing financial interests.

Correspondence should be addressed to either of the following: Dr Antony Czarnecki or Dr Pascal Legendre, Institut National de la Santé et de la Recherche Médicale Unité Mixte de Recherche S1130, Centre National de la Recherche Scientifique Unité Mixte de Recherche 8246, Université Pierre et Marie Curie, Bâtiment B, Etage 2, Boîte postale 37, 7 quai Saint Bernard, 75005 Paris, France, E-mail: antony.czarncki@sorbonne-universite.fr or pascal.legendre@inserm.fr

Cite as: J. Neurosci ; 10.1523/JNEUROSCI.3203-17.2018

Alerts: Sign up at www.jneurosci.org/cgi/alerts to receive customized email alerts when the fully formatted version of this article is published.

Accepted manuscripts are peer-reviewed but have not been through the copyediting, formatting, or proofreading process.

1 **Persistent sodium current drives excitability of immature Renshaw cells in**
2 **early embryonic spinal networks**

3
4 **Abbreviated title:** I_{Nap} drives the excitability of newborn V1^R

5
6
7 **Juliette Boeri**^{a,1}, **Hervé Le Corrond**^{a,b,1}, **François Xavier Lejeune**^a, **Barbara Le Bras**^a,
8 **Christine Mouffle**^a, **Monara Kaelle S.C. Angelim**^a, **Jean Marie Mangin**^a, **Pascal**
9 **Branchereau**^{c,d}, **Pascal Legendre**^{a,1}, **Antony Czarnecki**^{a,1}

10
11 ^a INSERM, UMR_S 1130, CNRS, UMR 8246, Neuroscience Paris Seine, Institute of Biology
12 Paris Seine, 75005 Paris, France. Sorbonne Univ, UPMC Univ Paris 06, UM CR18, 75005
13 Paris, France.

14 ^b Univ Angers, 49000 Angers, France.

15 ^c Univ. Bordeaux, INCIA, UMR 5287, F-33615 Pessac, France.

16 ^d CNRS, INCIA, UMR 5287, F-33615 Pessac, France.

17
18 Correspondence should be addressed to either of the following: Dr Antony Czarnecki or Dr
19 Pascal Legendre, Institut National de la Santé et de la Recherche Médicale Unite Mixte de
20 Recherche S1130, Centre National de la Recherche Scientifique Unité Mixte de Recherche
21 8246, Université Pierre et Marie Curie, Bâtiment B, Etage 2, Boîte postale 37, 7 quai Saint
22 Bernard, 75005 Paris, France, E-mail: antony.czarnecki@sorbonne-universite.fr or
23 pascal.legendre@inserm.fr.

24
25 **Number of pages:** 38

26
27 **Number of figures:** 10

28
29 **Number of tables:** 2

30
31 **Number of words:**

32 Abstract: 250

33 Introduction: 641

34 Discussion: 1492

35
36 **Acknowledgements:**

37 We thank Elim Hong for helpful discussion. This work was supported by FRM grant
38 DEQ20160334891, AFM Grant 18564, the Institut National de la Santé et de la Recherche
39 Médicale, and the Centre National de la Recherche Scientifique. The authors declare no
40 competing financial interests.

41 ¹J. B., H. L., P. L. and A. C. contributed equally to this work.

42

43 **ABSTRACT**

44

45 Spontaneous network activity (SNA) emerges in the spinal cord (SC) before the formation of
46 peripheral sensory inputs and central descending inputs. SNA is characterized by recurrent
47 giant depolarizing potentials (GDPs). Because GDPs in motoneurons (MNs) are mainly
48 evoked by prolonged release of GABA, they likely necessitate sustained firing of
49 interneurons. To address this issue we analyzed, as a model, embryonic Renshaw cell ($V1^R$)
50 activity at the onset of SNA (E12.5) in the embryonic mouse SC (both sexes). $V1^R$ are one of
51 the interneurons known to contact MNs, which are generated early in the embryonic SC.
52 Here, we show that $V1^R$ already produce GABA in E12.5 embryo, and that $V1^R$ make
53 synaptic-like contacts with MNs and have putative extrasynaptic release sites, while paracrine
54 release of GABA occurs at this developmental stage. In addition, we discovered that $V1^R$ are
55 spontaneously active during SNA and can already generate several intrinsic activity patterns
56 including repetitive-spiking and sodium-dependent plateau potential that rely on the presence
57 of persistent sodium currents (I_{NaP}). This is the first demonstration that I_{NaP} is present in the
58 embryonic SC and that this current can control intrinsic activation properties of newborn
59 interneurons in the SC of mammalian embryos. Finally, we found that 5 μ M riluzole, which is
60 known to block I_{NaP} , altered SNA by reducing episode duration and increasing inter-episode
61 interval. Because SNA is essential for neuronal maturation, axon pathfinding and
62 synaptogenesis, the presence of I_{NaP} in embryonic SC neurons may play a role in the early
63 development of mammalian locomotor networks.

64 **SIGNIFICANCE STATEMENT**

65 The developing spinal cord (SC) exhibits spontaneous network activity (SNA) involved in the
66 building of nascent locomotor circuits in the embryo. Many studies suggest that SNA depends
67 on the rhythmic release of GABA, yet intracellular recordings of GABAergic neurons have
68 never been performed at the onset of SNA in the SC. We first discovered that embryonic
69 Renshaw cells ($V1^R$) are GABAergic at E12.5 and spontaneously active during SNA. We
70 uncover a new role for persistent sodium currents (I_{NaP}) in driving plateau potential in $V1^R$
71 and in SNA patterning in the embryonic SC. Our study thus sheds light on a role for I_{NaP} in
72 the excitability of $V1^R$ and the developing SC.

73

74 **INTRODUCTION**

75 A remarkable feature of the developing central nervous system (CNS) is its capacity to
76 generate spontaneous network activity (SNA) at the end of neuronal migration. SNA occurs in
77 the absence of any external inputs and is not experience-driven or use-dependent (Moody,
78 1998; Feller, 1999). SNA has been described as playing an essential role in several areas of
79 the developing CNS, including the neocortex, the thalamus, the hippocampus, the locus
80 coeruleus, the retina and the spinal cord (Landmesser and O'Donovan, 1984; Ben-Ari et al.,
81 1989; Garaschuk et al., 1998; Feller, 1999; Garaschuk et al., 2000; Gust et al., 2003; Corlew
82 et al., 2004; Marder and Rehm, 2005; Myers et al., 2005; Gonzalez-Islas and Wenner, 2006;
83 Hanson et al., 2008; Rockhill et al., 2009; Watt et al., 2009). SNA regulates the development
84 of neural circuits by influencing synaptogenesis, neuronal maturation, axonal guidance and
85 axonal pathfinding (Zhang and Poo, 2001; Hanson et al., 2008; Kirkby et al., 2013).

86 In the embryonic spinal cord (SC), SNA is characterized by long-lasting bursts of action
87 potentials (APs) occurring every 2-4 min that can propagate along the cord (Hanson and
88 Landmesser, 2003). SNA occurs at the onset of synaptogenesis at E12.5, before the
89 emergence of functional neuromuscular junction and the formation of sensory and supra-
90 spinal inputs (Hanson and Landmesser, 2003). Bursts of APs recorded on ventral roots
91 (Hanson and Landmesser, 2003) or in the whole SC (Yvert et al., 2004) are long-lasting
92 episodes characterizing SNA in the embryonic SC. We previously showed that most
93 individual motoneurons (MNs) only generate a single AP during each episode of SNA
94 (Czarnecki et al., 2014) and we demonstrated that acetylcholine (ACh) release could not
95 directly synchronize MN firing during SNA as MNs do not express functional acetylcholine
96 receptors (Czarnecki et al., 2014). Therefore, MNs must rely on other mechanisms to
97 synchronize their firing during SNA. We have recently shown that MN activity occurring
98 during SNA at the onset of synaptogenesis (E12.5) is generated by giant depolarizing
99 potentials (GDPs) involving a massive and long-lasting release of GABA, as well as a

100 moderate release of glutamate and glycine (Czarnecki et al., 2014). It is therefore likely that
101 newborn GABAergic interneurons (INs) play an essential role in the generation of the
102 sustained episodes of depolarization necessary to synchronize MN firing during SNA.

103 To gain insight into the excitability pattern of spinal GABAergic INs involved in the
104 release of GABA during SNA, we used multiple approaches to examine the intrinsic
105 activation properties of immature Renshaw cells ($V1^R$) in the lumbar SC. Renshaw cells are
106 known to regulate MN activity in the adult through recurrent synaptic inhibition (Eccles et al.,
107 1956) and play an important role in the regulation of SC activity at late developmental stages
108 in the chicken embryo (Wenner and O'Donovan, 2001). $V1^R$ are the first V1 INs to be
109 generated during neurogenesis in the mouse embryo (Benito-Gonzalez and Alvarez, 2012).
110 From E9.5 to E12.5, $V1^R$ migrate toward their final location between MN columns and the
111 ventrolateral funiculus (Benito-Gonzalez and Alvarez, 2012; Alvarez et al., 2013). Because
112 glycine, unlike GABA, is nearly absent in SC INs of E12.5 mouse embryo (Allain et al.,
113 2004, 2006; Scaini et al., 2010), $V1^R$ are likely to be GABAergic neurons at the early
114 developmental stage.

115 Here, we show that, like MNs, $V1^R$ display GDPs during SNA at E12.5. However, we
116 discovered that, unlike MNs, most $V1^R$ are able to produce repetitive spiking or sodium-
117 dependent plateau potentials in response to GDPs (Czarnecki et al., 2014). Remarkably, these
118 sustained discharges depend on the presence of a persistent sodium current (I_{Nap}). In addition,
119 we also demonstrate that I_{Nap} already has important functions at the onset of SNA. Inhibition
120 of I_{Nap} alters SNA episode duration and inter-episode interval duration, which reveals that the
121 ability of embryonic SC neurons to generate sustained discharge is required for a correct SNA
122 pattern (Hanson and Landmesser, 2006).

123

124 **MATERIALS AND METHODS**125 ***Isolated spinal cord preparation***

126 These experiments were performed in accordance with European Community guiding
127 principles on the care and use of animals (86/609/CEE, CE Off J no. L358, 18 December
128 1986), French decree no. 97/748 of October 19, 1987 (J Off République Française, 20
129 October 1987, pp. 12245-12248) and recommendations from the CNRS. We used
130 GAD67eGFP knock-in mice to visualize putative GABAergic INs (Tamamaki et al., 2003).
131 Briefly, a cDNA encoding enhanced GFP (eGFP) was targeted to the locus encoding the gene
132 Gad1. GAD67 is a rate-limiting enzyme of GABA biosynthesis and is known to be a marker
133 for GABAergic neurons (Le Corrionc et al. 2011). To obtain E12.5 GAD67-eGFP embryos, 8-
134 to 12-week-old wild-type Swiss female mice were crossed with heterozygous GAD67-eGFP
135 Swiss male mice. HB9-eGFP mouse embryos were used to visualize MNs (Wichterle et al.,
136 2002). To obtain E12.5 transgenic HB9-eGFP embryos, 8- to 12-week-old wild-type Swiss
137 female mice were crossed with heterozygous HB9-eGFP C57BL/6Jrj male mice.

138 269 embryos obtained from 152 pregnant mice were used. Isolated embryonic mouse
139 SCs were obtained as previously described (Delpy et al., 2008; Scain et al., 2010). Briefly,
140 pregnant mice were anesthetized by intramuscular injection of a mix of ketamine and xylazine
141 and sacrificed using a lethal dose of CO₂. Embryos of either sex were removed and the SC
142 was isolated from eGFP-positive embryos. Whole SCs were maintained in an artificial
143 cerebrospinal fluid (ACSF) containing 135 mM NaCl, 25 mM NaHCO₃, 1 mM NaH₂PO₄, 3
144 mM KCl, 11 mM glucose, 2 mM CaCl₂, and 1 mM MgCl₂ (307 mosmol/kg H₂O),
145 continuously bubbled with a 95% O₂-5% CO₂ gas mixture.

146

147 ***Whole-cell recordings and analysis***

148 The isolated SC was placed in a recording chamber and continuously perfused (2
149 mL/min) at room temperature (20-24°C) with the oxygenated ACSF described above. Whole-

150 cell patch-clamp recordings of lumbar spinal V1^R and MNs were carried out under direct
151 visualization using an infrared-sensitive CCD video camera.

152 In the SC of GAD67eGFP mouse embryos, eGFP neurons were detected using UV
153 light. MNs were identified by their size, their location in the ventral area of the SC
154 parenchyma (Czarnecki et al., 2014) and by the lack of eGFP expression. These neurons
155 localized in this SC area express the MN transcription factors *Islet1/2*, as shown in a previous
156 study (Scain et al, 2010). Recorded eGFP interneurons were localized in the ventrolateral area
157 of the SC at the marginal zone between motor columns and the ventral funiculus, which is the
158 known location of developing V1^R (Stam et al., 2012). To confirm V1^R identity, recorded
159 cells were filled with neurobiotin (0.5-1 mg/mL) and stained with an antibody directed against
160 Foxd3. Foxd3 is a specific transcription factor of V1 INs (Dottori et al., 2001; Stam et al.,
161 2012) and the hallmark of V1^R localized in the ventrolateral area of the embryonic SC (Carr et
162 al., 1998; Benito-Gonzalez and Alvarez, 2012).

163 Whole-cell patch-clamp electrodes were pulled from thick-wall borosilicate glass using
164 a Brown-Flaming puller (Sutter Instrument Co., USA). The tip of the electrode was fire-
165 polished using a microforge (Narishige, Japan). Patch-clamp electrodes had resistances of 4-7
166 M Ω . The electrode was filled with a solution containing (in mM): 96.4 K methanesulfonate,
167 33.6 KCl, 4 MgCl₂, 4 Na₂ATP, 0.3 Na₃GTP, 10 EGTA, and 10 HEPES (pH 7.2; 290
168 mosmol/kg-H₂O). Using these potassium methanesulfonate solutions, the equilibrium
169 potential for chloride ions (E_{Cl}) \approx -30 mV was close to the physiological values measured at
170 E12.5 on spinal MNs (Delpy et al., 2008). The junction potential (6.6 mV) was systematically
171 corrected offline. In some voltage-clamp experiments, the electrode contained: (in mM) 130
172 CsCl, 4 MgCl₂, 4 Na₂ATP, 10 EGTA and 10 HEPES (pH 7.2; 290 mosmol/kg-H₂O).

173 Signals were recorded using Axopatch 200B or Multiclamp 700B amplifiers (Molecular
174 Devices, USA). Data were low-pass filtered (2 kHz), digitized (20 kHz) online using a
175 Digidata 1440A interface and acquired using PClamp 10.5 software ([pClamp](#),

176 RRID:SCR_011323). Analyses were performed off-line using PClamp 10.5 software and
177 Axograph X.1.6.4 (Axograph , RRID:SCR_014284).

178 In voltage-clamp or current-clamp experiments, neurons were recorded at a holding
179 potential (V_h) of -60 mV. Series resistance (10-20 M Ω) was monitored throughout the
180 experiments and was 50-80% compensated. Data were discarded if series resistance varied by
181 more than $\approx 30\%$ from the initial value. In current-clamp mode, $V1^R$ intrinsic discharge
182 patterns were elicited using depolarizing current steps (from 0 to ≈ 50 pA, 2-10 pA
183 increments depending on the input resistance of the cell, 2 seconds) or depolarizing current
184 triangular-ramp (from 0 to ≈ 50 pA, 5 pA increments, 20 seconds) with an 8-second interval
185 to ensure that the membrane potential returned to baseline V_h . In voltage-clamp mode, whole-
186 cell currents were elicited by a depolarizing voltage ramp. The 70 mV/s speed was chosen to
187 elicit and measure persistent inward currents (I_{Nap}) (Huang and Trussell, 2008). Subtraction of
188 the current evoked by the voltage ramp in the presence of 1 μ M TTX to control voltage ramp-
189 evoked current revealed I_{Nap} .

190 Action potentials or plateau potentials were analyzed based on the following parameters
191 during a 2-second current step: threshold potential, peak amplitude, half amplitude duration,
192 rate of rise of events (by dividing the amplitude of the event by the duration from its onset to
193 the peak; 2 seconds step width).

194 Boltzmann functions were used to describe I_{Nap} activation on current evoked by voltage
195 ramp. For the fit current (20 kHz sampling 2 KHz filter):

196

$$197 \quad G = G_{MAX}/(1+\exp(-(V-V_{HALF})/k))$$

198

199 where G is conductance in nS, G_{Max} is the maximal conductance, V is the potential in mV,
200 V_{HALF} is the voltage for half-maximal activation in mV, and k is the slope factor in mV.

201 Threshold for activation I_{Nap} was determined by eye from Boltzmann curves.

202

203 ***Extracellular recordings***

204 In the same experimental conditions as for whole-cell recordings, spontaneous activity
205 was recorded extracellularly from E12.5 SCs using glass electrodes. Extracellular electrodes
206 were placed under visual control on the superficial part of the ventral horn both at the cervical
207 and the lumbar levels. Targeted networks likely include MNs as well as surrounding INs
208 (Czarnecki et al., 2014). Electrodes were connected to a high-gain a.c. amplifier (ISO-
209 DAM8A-4 Bio-amplifier System, World Precision Instruments Ltd, Stevenage, UK). Filtered
210 (Filter cutoff frequency: 0.3-3 kHz) raw signals were integrated off-line and analyzed using
211 Spike2 software ([Spike2 Software](#), RRID:SCR_000903). Changes in burst duration and
212 maximum instantaneous frequency were calculated from cervical and lumbar recordings.

213

214 ***Pharmacological agents***

215 During patch-clamp recordings, drugs were applied using 0.5 mm diameter quartz
216 tubing positioned 50 μm away from the recording area under direct visual control. The quartz
217 tubing was connected using a manifold to 6 solenoid valves linked with 6 reservoirs.
218 Solutions were gravity-fed into the quartz tubing. Drug application was controlled using a
219 VC-8 valve controller (Warner Instruments, USA). The following pharmacological agents
220 were used: tetrodotoxin (TTX) (1 μM , Alomone, Israel) and riluzole (5-10 μM Tocris
221 Bioscience, UK). Both were dissolved in the bath solution.

222

223 ***Immunohistochemistry***

224 All primary antibodies used and their respective dilutions are listed in Table 1. E12.5
225 embryos were collected from pregnant females. Once dissected out of their yolk sac, these
226 embryos were immediately immersion-fixed in phosphate buffer (PB 0.12 M) with 4%
227 paraformaldehyde (PFA; freshly prepared in PB, pH 7.4) for 1 h at 4°C. Embryos were then

228 rinsed with PB and cryoprotected in PB-15% sucrose at 4°C for 24 h and then in PB-30%
229 sucrose at 4°C for 24 h. Embryos were embedded in OCT medium (VWR, Fontenay-sous-
230 Bois, France) and quickly frozen. Serial sections 20 µm thick were collected onto slides using
231 a cryostat. Immunostaining was processed on SC transverse sections and on whole SC post-
232 recording to confirm IN identity. To reveal neurobiotin-labeled cells, SCs were fixed for 1 h
233 in 4% PFA and were then incubated in 0.12 M PB at 4°C until immunohistochemical studies.
234 Tissues (embryo slices and whole SC) were thawed at room temperature, washed in PBS,
235 incubated in NH₄Cl (50 mM) diluted in PBS for 20 min and then permeabilized for 30 min in
236 a blocking solution (10% goat serum in PBS) with 0.2% Triton X-100 and then for 48 h at
237 4°C with the primary antibodies, which were diluted in the 0.2% Triton X-100 blocking
238 solution. Slices or whole SCs were then washed in PBS and incubated for 2 h at RT in the
239 secondary antibodies (diluted at 1/1000 in the 0.2% Triton X-100 blocking solution): Alexa
240 Fluor 405 (Thermo Fisher Scientific Cat# A-31556, RRID:AB_221605) or 647 goat anti-
241 rabbit (Thermo Fisher Scientific Cat# A-21244, RRID:AB_2535812); Alexa Fluor 594 goat
242 anti-guinea pig (Thermo Fisher Scientific Cat# A-11076, RRID:AB_2534120); Alexa Fluor
243 649 donkey anti-guinea pig (Jackson ImmunoResearch Labs Cat# 706-605-148,
244 RRID:AB_2340476); Alexa Fluor 594 goat anti-mouse (Thermo Fisher Scientific Cat# A-
245 11005, RRID:AB_2534073); Alexa Fluor 488 goat anti-chicken (Thermo Fisher Scientific
246 Cat# A-11039, RRID:AB_2534096) and streptavidin-conjugated Alexa Fluor 405 (1:1000,
247 Thermo Fisher Scientific Cat# S32351). After washing in PBS, slides or whole SCs were
248 dried and mounted in Mowiol medium (Millipore, Molsheim, France).

249

250 *Confocal microscopy and image analysis*

251 Preparations were analyzed using a Leica SP5 confocal microscope. Immunostaining
252 was observed using a 40X oil-immersion objective with a numerical aperture of 1.25, as well
253 as with a 63X oil-immersion objective with a numerical aperture of 1.32 and a 4X digital

254 zoom magnification. Serial optical sections were obtained with a Z-step of 1 μm (40X) and
255 0.2-0.3 μm (63X). Images (1024x1024; 12-bit color scale) were stored using Leica software
256 LAS-AF and analyzed using ImageJ 1.5 softwares ([Wright Cell Imaging Facility](#),
257 RRID:SCR_008488). Colocalization of synaptophysin staining with calbindin staining, eGFP
258 staining (MNs; HB9eGFP mouse embryos) or neurobiotin staining was assessed in 3 axes
259 using a single confocal slice and X and Y orthogonal views of the stack (ImageJ 1.5).

260

261 ***Sniffer recordings.***

262 To make a “sniffer” electrode (Young and Poo, 1983) for GABA, an outside-out patch
263 was pulled from a transfected HEK293 cell line expressing the GABA_AR subunits $\alpha 3\beta 2\gamma 2$
264 (kindly provided by Michel Partiseti, Sanofi Advantis R&D LGCR/LIT, France). This
265 GABA_AR is highly specific for GABA and is characterized by slow desensitization, which
266 makes it a good sensor for GABA paracrine release (Barberis et al., 2007). As a control, the
267 electrode was first positioned outside the SC to verify any GABA contamination in the
268 recording medium. The electrode was then pushed inside the SC and positioned within the
269 motoneuronal area and the ventral funiculi. Outside-out patch-clamp electrodes (5-10 M Ω)
270 were pulled from thick-wall borosilicate glass, fire-polished and filled with (in mM): CsCl
271 130, MgCl₂ 4, Na₂ATP 4, EGTA 10, HEPES 10 (pH 7.2, osmolarity 290 mosmol/kg-H₂O).
272 Single channel currents were recorded using an Axopatch 200B amplifier (Molecular
273 Devices, USA). Recordings were filtered at 10 kHz, sampled at 50 kHz and stored on a PC
274 computer. Membrane potential was held at -50 mV throughout the experiment. Analysis of
275 the sniffer currents was performed using Axograph X.1.6.4 software.

276 Human embryonic kidney 293 cells (HEK293) were maintained in a 95% air - 5% CO₂
277 humidified incubator, at 35°C, in Dulbecco’s modified Eagle’s medium supplemented with
278 0.11 g/L sodium pyruvate, 6 g/L D-glucose, 10% (v/v) heat-inactivated fetal bovine serum (all
279 from Gibco BRL). Cells were passaged every 5-6 days (up to maximum 20 times). For

280 electrophysiological recordings, cells were seeded onto glass coverslips coated with poly-L-
281 ornithine (0.1 mg/mL).

282 ***Statistics***

283 All values were expressed as mean \pm standard deviation. Statistical significance was
284 assessed by the non-parametric Kruskal-Wallis test with Dunn's post tests, Mann-Whitney
285 test and Wilcoxon matched pairs test (GraphPad Prism 5.0 Software, USA). Significance was
286 determined as $P < 0.05$ (*), $P < 0.01$ (**) or $P < 0.001$ (**).

287 **RESULTS**288 *V1^R are identified with calbindin, Foxd3 and MafB at the onset of SNA.*

289 In the present study, we used GAD67-enhanced green fluorescent protein (eGFP)
290 knock-in mice (Tamamaki et al., 2003) to visualize putative GABAergic INs (Figures 1A1,
291 1B1 and 1C1). V1^R can be unambiguously identified by their characteristic position in the
292 ventral horn both in the adult (Geiman et al., 2000) and in the embryo (Sapir et al., 2004;
293 Stam et al., 2012). Most V1^R were localized between the ventral border of MN columns and
294 the ventral funiculi. To identify V1^R in the lumbar SC of E12.5 GAD67eGFP embryos, we
295 first performed immunostaining using anti-calbindin, anti-Foxd3 and anti-MafB antibodies
296 (Figure 1). Calbindin is a calcium-binding protein exclusively expressed by V1^R when
297 looking in the ventrolateral area of the SC between the MN columns and the funiculus (Stam
298 et al., 2012). The forkhead transcription factor Foxd3 controls the early phase of V1^R
299 differentiation, whereas MafB is required to maintain V1^R at later developmental stages, and
300 both are therefore expressed at E12.5 in V1^R (Stam et al., 2012). At E12.5 INs located in the
301 ventrolateral marginal zone between the motor columns and the ventral funiculi express
302 Foxd3 (Figures 1A2, 1B2 and 1C2) and calbindin (Figures 1A3 and 1B3), as previously
303 described (Stam et al., 2012; Benito-Gonzalez et al, 2012). Foxd3⁺ INs were also observed in
304 neurons positioned dorsally to the motor columns (Figures 1A2 and 1B2). However, these INs
305 were not stained by calbindin antibody, hence this population of INs was not included in our
306 study. In the V1^R area, double immunostaining (Figures 1A4 and 1B4) indicated that 81.7 ±
307 15.0% of Foxd3⁺ INs localized in the ventral marginal zone were also immunoreactive to
308 calbindin at E12.5 (n=4 embryos, 2 sections/embryo). To ensure that all Foxd3⁺ INs localized
309 in the area are V1^R, we performed double immunostaining using anti-Foxd3 and anti-MafB
310 antibodies (Figures 1C). We found that 100% of Foxd3⁺ eGFP⁺ INs localized in the ventral
311 marginal zone were also immunoreactive to anti-MafB antibody (n = 4 embryos, 2
312 sections/embryo), thus confirming their V1^R fate (Figure 1C4). It should also be noted that at

313 this developmental stage we detected MafB⁺ eGFP⁻ neurons localized within the motor
314 columns (Figures 1C1 and 1C3) that are likely MNs (Stam et al., 2012). Therefore, we used
315 Foxd3 immunostaining to confirm that the recorded IN belonged to the V1^R population
316 (Figures 1D1, 1D2, 1D3 and 1D4). Whereas Calbindin is a good marker for V1^R, it was not
317 used to identify recorded V1^R because of cytoplasm-calbindin dilution complications during
318 whole-cell recording (Muller et al., 2005), caused by the high nucleus/cytoplasm volume ratio
319 in embryonic neurons.

320

321 ***V1^R already produce GABA at E12.5.***

322 As calbindin is localized within the cytoplasm of V1^R, we used calbindin
323 immunostaining to visualize V1^R morphology (Stam et al., 2012). $96.6 \pm 7.2\%$ of calbindin⁺
324 neurons in the ventrolateral marginal zone were also eGFP⁺ in E12.5 GAD67eGFP knock-in
325 mouse embryos (n = 4 embryos, 2 sections/embryo), which could suggest that most V1^R are
326 likely to produce GABA at this developmental stage. To determine to what extent V1^R already
327 produce GABA at E12.5, we performed double immunostaining using anti-calbindin and anti-
328 GABA antibodies (Figures 2A and 2B). We found that $90.1 \pm 10.5\%$ (n = 8 embryos, 2
329 sections/embryo) of calbindin⁺ INs localized in the ventrolateral marginal zone (Figures 2A2
330 and 2B2) were also immunoreactive to GABA antibody (Figures 2A3, 2A4, 2B3 and 2B4),
331 suggesting that V1^R already produced enough GABA to be detected by
332 immunohistochemistry at E12.5.

333 It is important to note that many eGFP⁺ GABA⁻ INs were detected within the ventral
334 parenchyma at E12.5, as previously observed (Allain et al., 2004). This could result from the
335 production of the GAD67 splice variant GAD25. At early developmental stages, GAD1 first
336 encodes the truncated 25-kDa leader (GAD25) without GAD enzymatic activity and then the
337 enzymatically active protein GAD44 (see for review (Le-Corronc et al., 2011)). These two
338 GAD isoforms are down-regulated during neuronal differentiation concomitantly with up-

339 regulation of GAD67 expression.

340

341 ***Synaptic-like contacts are detected between $V1^R$ and MNs at the onset of SNA***

342 At E12.5, $V1^R$ axons are localized in ventral funiculi and extend for a few segments
343 without forming collateral branches entering the motor columns (Alvarez et al., 2013). The
344 first evidence for collateral $V1^R$ axons innervating the soma of lumbar MNs was found at
345 E15.5 only while synaptic-like connections from MNs onto the $V1^R$ cell body were already
346 observed at E12.5 (Alvarez et al., 2013). Accordingly, it was proposed that MNs can control
347 $V1^R$ activity at E12.5 while $V1^R$ are unable to control MN activity at this time point (Alvarez
348 et al., 2013). However, it should be noted that synaptophysin staining was found mainly in the
349 ventral funiculus at E12.5 (Figure 3A1) (Alvarez et al., 2013; Czarnecki et al., 2014), where
350 IN axonal projections and MN dendrite-like processes were observed (Czarnecki et al., 2014).
351 Accordingly, we hypothesized that $V1^R$ already make some synaptic-like contacts with MN
352 projections within the ventral funiculus.

353 To address this issue we first performed multiple immunostaining using anti-synaptophysin
354 antibody (putative release site), anti-calbindin antibody ($V1^R$) and anti-eGFP antibody on
355 coronal sections of the SC HB9eGFP mouse embryos to visualize MNs (Figures 3A2, 3A3,
356 3A4, 3B1, 3B2 and 3B3). As shown in Figure 3B3, many calbindin⁺ fibers were apposed to
357 MN neurites (eGFP staining) within the ventral funiculus. We found 21.7 ± 8.4
358 synaptophysin⁺ punctates within calbindin⁺ fibers apposed to MN neurites per hemi section in
359 coronal slices (n = 9; 5 embryos) (Figures 3B1, 3B2 and 3B3; inserts, arrow). Conversely,
360 synaptophysin punctates were also found in MN fibers (eGFP⁺) apposed to calbindin⁺ fibers
361 (Figures 3B1, 3B2 and 3B3; insert, arrow head), which indicate the presence of MN putative
362 release sites apposed to $V1^R$ within the ventral funiculus. We also found synaptophysin
363 punctates within calbindin⁺ fibers that were not apposed to MN neurites (Figures 3B1, 3B2
364 and 3B3; barred arrow). This may indicate the presence of non-synaptic release sites and/or

365 that $V1^R$ can make contact with fibers of neurons other than MNs. To further confirm the
366 presence of $V1^R$ synaptic-like contacts on MNs, we performed multiple immunostaining using
367 anti-synaptophysin antibody (putative release site) and anti-eGFP antibody on isolated SC
368 after patch-clamp injection of neurobiotin in $V1^R$ (Figures 3C). Recorded INs (eGFP negative)
369 in eGFP HB9 embryos were identified as $V1^R$ using Foxd3 immunostaining (Figure 3C1;
370 insert). We found 3 to 5 putative release sites per $V1^R$ ($n = 4$ cells) that were apposed to MN
371 fibers within the ventral funiculus (Figures 3C1, 3C2, 3C3 and 3C4). We did not find any
372 release site within the $V1^R$ axonal growth cone (data not shown).

373

374 ***Paracrine release of GABA occurred in the SC of E12.5 mouse embryos.***

375 Paracrine release of GABA may occur from non-synaptic release sites and/or may
376 reflect neurotransmitter spillover of GABA from immature synapses (Safiulina and
377 Cherubini, 2009). Therefore, we hypothesized that GABA release can occur at this
378 developmental stage. To detect the presence of GABA paracrine release, we used the sniffer
379 technique (Scain et al., 2010). Outside-out patches from HEK cells expressing the $GABA_A$ R
380 subunits $\alpha 3\beta 2\gamma 2$ were used as a “sniffer” to detect the presence of GABA in the extracellular
381 space (Figure 4 A1). When inserting the sniffer electrode in the vicinity of MNs, we did not
382 detect any $GABA_A$ R, thus indicating that basal GABA concentration is below the detection
383 threshold of the sniffer patch (data not shown). The possibility of evoking GABA release, and
384 hence $GABA_A$ R activation, by inducing a global cell membrane depolarization was tested
385 using bath application of 30 mM KCl (Scain et al., 2010; Czarnecki et al., 2014). Increasing
386 $[K^+]_o$ evoked a significant $GABA_A$ R activation in the sniffer patch ($n = 9$), indicating that
387 GABA can be released in the extracellular space in response to cell membrane depolarization
388 (Figure 4 A1). We estimated the concentration of released GABA around MNs by comparing
389 the peak amplitude of the sniffer response evoked by KCl application to sniffer responses
390 evoked by exogenous application of 3, 10 and 30 μ M GABA onto the same outside-out patch

391 (n = 9). We found that the GABA concentration accounting for GABA_AR activity evoked by
392 KCl application was close to 3 μ M (Figure 4 A2). Although the estimated concentration of
393 non-synaptic release of GABA was relatively low, the exogenous application of 3 μ M GABA
394 in the presence of 1 μ M TTX was sufficient to evoke a 20.6 ± 6.1 mV MN depolarization (V_h
395 = -60 mV; $E_{Cl} = -30$ mV; n = 7) (Figures 4B2).

396

397 ***V1^R exhibit heterogeneous excitability patterns at the onset of SNA.***

398 Spontaneous or evoked RC activity was assessed using whole-cell current-clamp
399 recordings and the open-book SC preparation (Scain et al., 2010). To determine the identity of
400 recorded INs, GAD67eGFP neurons were filled with neurobiotin (≈ 1 mg/mL) in combination
401 with post-hoc Foxd3 staining (Figures 1D). At E12.5, V1^R had a whole-cell capacitance of
402 13.7 ± 3.8 pF (n = 192) and an input resistance of 1242 ± 620 M Ω (n = 192). Spontaneous
403 activity recorded in 37 V1^R was characterized by recurrent GDPs (Figure 5), occurring every
404 3.7 ± 2.4 min (n = 30), similar to what has been observed in MNs (~ 3 min) (Czarnecki et al.,
405 2014). Interestingly, in 21.6% (n = 8/37) of the recorded V1^R, GDPs evoked long-lasting
406 depolarizing plateau potentials (Figure 5A), while 37.8% (n = 14/37) of the recorded V1^R had
407 the ability to spike repetitively during GDPs (Figure 5B). Plateau potentials had an absolute
408 amplitude of 53.4 ± 11.5 mV (n = 8) and a half amplitude duration ranging from 0.12 to 0.86
409 s (0.44 ± 0.22 s; n = 8). In 16.2% (n = 6/37) of the recorded V1^R, GDPs evoked a single spike
410 or a doublet (figure 5C), while the remaining 24.3% (n = 9/37) of the recorded V1^R did not
411 spike during GDPs (data not shown). These data show that V1^R can generate various
412 spontaneous activity patterns and raise the question of their intrinsic activation properties.

413 To analyze the intrinsic activation properties of embryonic V1^R, we depolarized the
414 cells from a holding potential of -60 mV using 2 s step current pulses or 20 s depolarizing
415 current ramps. At E12.5, all V1^R were excitable (n = 164), but depolarizing current injections
416 triggered various and complex excitability patterns (Figure 6). 28.7% (n = 47/164) of the

417 analyzed $V1^R$ were able to generate 1 to 3 action potentials (APs) in response to
418 suprathreshold depolarizing steps (Figure 6A). When a depolarizing ramp was applied, only
419 fast membrane potential oscillations of small amplitude were observed. We called these $V1^R$,
420 SS- $V1^R$, (“single” spiking $V1^R$). In contrast, 21.2% ($n = 36/164$) of the recorded $V1^R$ were
421 able to generate long-lasting events defined as plateau potentials in response to depolarizing
422 current pulses and in response to depolarizing current ramps. These plateau potentials were
423 all-or-none events (Figure 6B). They can be evoked by long depolarizing pulses (2s) (Figure
424 6B) and short depolarizing current pulses (Figure 6F2). They had a half amplitude duration of
425 ≈ 700 ms and an absolute peak amplitude of ≈ 3 mV (Table 2). Remarkably, these plateau
426 potentials were sodium-dependent events as they were fully blocked by the application of 1
427 μ M TTX (Figure 6F1). Unlike SS- $V1^R$, these $V1^R$ can generate repetitive plateau potentials
428 when depolarized by a suprathreshold depolarizing current ramp (Figure 6B). We called these
429 $V1^R$, PP- $V1^R$ (plateau potential $V1^R$). A third group of $V1^R$ (41.5%; $n = 68/164$) was
430 identified based on their ability to generate repetitive AP firing in response to suprathreshold
431 depolarizing current steps or to depolarizing current ramps. In these cells, APs had a half
432 amplitude duration ≈ 13 ms (Table 2). We called these $V1^R$, RS- $V1^R$ (repetitive spiking $V1^R$)
433 (Figure 6C). Finally, a fourth group of cells (8.5%; $n = 14/164$) was determined according to
434 their ability to generate both APs and plateau potential-like events (Figure 6D). We called
435 these $V1^R$, ME- $V1^R$ (mixed event $V1^R$). SS- $V1^R$ are unlikely to be dying neurons.
436 Developmental cell death (DCD) of V1 INs occurs after E14.5 in mouse embryos (Prasad et
437 al., 2008) and SS- $V1^R$ passive electrical properties did not differ from those of more active
438 $V1^R$ (Table 2).

439 Considering that the different types of intrinsic activation pattern may reflect a
440 continuum between a single spike and a plateau potential, we chose to focus our study on the
441 three clear patterns of intrinsic activation, SS- $V1^R$, RS- $V1^R$ and PP- $V1^R$, and to not study the
442 mixed regime in depth. Table 2 summarizes passive and active intrinsic electrical properties

443 of recorded SS-V1^R, RS-V1^R and PP-V1^R. Note that the difference in intrinsic excitability in
444 these different classes of V1^R is not due to difference in their membrane resistance ($P > 0.1$).

445 These results reveal that V1^R can have different regimes of activity in the embryonic SC
446 at the onset of synaptogenesis and SNA (E12.5) (Scain et al., 2010; Czarnecki et al., 2014).

447

448 ***Sustained discharge in embryonic V1^R depends on persistent sodium current.***

449 A key element in neurons, which exhibit sustained discharges, is the expression of
450 subthreshold slow-inactivating inward currents. Among these inward currents, the TTX-
451 sensitive persistent inward current (I_{Nap}) plays a fundamental role in controlling sustained
452 discharge in INs and MNs in the SC at postnatal developmental stages (Lee and Heckman,
453 1998; Kuo et al., 2006; Theiss et al., 2007; Ziskind-Conhaim et al., 2008).

454 To determine whether I_{Nap} is already expressed by V1^R in E12.5 mouse embryo, we
455 made whole-cell voltage-clamp recordings. In this set of experiments, the electrodes were
456 filled with a Cs-based intracellular solution to minimize contamination of the recorded current
457 by potassium currents. A test pulse from -100 to -20 mV evoked TTX-sensitive sodium
458 currents: a large amplitude transient current (I_{NaT}) followed by a smaller amplitude current
459 persisting over 0.5 s was also fully blocked by TTX (Figure 7A1, inset), which indicates the
460 presence of I_{Nap} . This also indicates that sodium-independent voltage-gated inward currents
461 were not detected at this developmental stage. To characterize I_{Nap} better, we used a slow
462 voltage ramp (70 mV/s) from -100 to +20 mV designed to inactivate transient currents
463 (Huang and Trussell, 2008). Subtraction of the trace after TTX application revealed the I_{Nap}
464 on the I-V curve (Figure 7A1). I_{Nap} was observed in all recorded RCs. We further investigated
465 the activation properties of the I_{Nap} . The Boltzmann fit of the voltage dependence of the I_{Nap}
466 generated by voltage ramps revealed a V_{half} of -22.9 ± 5.7 mV and a slope factor (k) of $7.0 \pm$
467 1.8 mV in RCs ($n = 8$) (Figure 7A2). In RCs, the I_{Nap} activated at $V_h = -67.4 \pm 6.2$ mV ($n = 8$)

468 and the mean persistent sodium conductance density (g_{Nap}/pF) was 41.8 ± 22.7 pS/pF ($n = 12$)
469 (Figure 7B).

470 To further confirm that this persistent inward current truly reflects the presence of I_{Nap} ,
471 we tested the effect of a low concentration of riluzole ($5 \mu\text{M}$), which is known to block I_{Nap}
472 (Urbani and Belluzzi, 2000). Indeed, $5 \mu\text{M}$ riluzole suppressed $81.5 \pm 14.6\%$ ($n = 15$; $P =$
473 0.0005) of the I_{Nap} in V1^{R} (Figure 7C), whereas at this low concentration riluzole only slightly
474 reduced the peak amplitude of I_{NaT} (see red arrows in Figure 7A1, inset). We confirmed on
475 MNs that this low concentration had a minimal effect on the sodium-dependent AP, which
476 was not the case when riluzole concentration was increased to $10 \mu\text{M}$ (Figures 8A and 8B1-
477 B3). AP amplitude was significantly reduced to $83.2 \pm 12.6\%$ of control in the presence of 5
478 μM riluzole ($n = 7$; $P = 0.008$), but was reduced to $67.5 \pm 17.0\%$ of control when riluzole
479 concentration was increased to $10 \mu\text{M}$ ($n = 7$, $P = 0.0078$). We then reasoned that the lack of
480 repetitive spiking or plateau potential activity observed in some V1^{R} might depend on a
481 reduced level of I_{Nap} . To test this hypothesis, we compared the presence of I_{Nap} in V1^{R} that
482 cannot generate repetitive spiking (SS- V1^{R}) with V1^{R} that can generate repetitive spiking
483 (RS- V1^{R}) and with V1^{R} generating plateau potentials (PP- V1^{R}). We developed a voltage- and
484 current-clamp recording protocol in a given neuron allowing us to associate the amplitude of
485 the I_{Nap} with the excitability pattern in each type of spinal neuron (K-methanesulfonate
486 intracellular solution) (Figure 9 A1-A4). The same voltage ramp (70 mV/s) was used as
487 described above. The I_{Nap} current was revealed by subtracting ramp-evoked current in the
488 presence of $1 \mu\text{M}$ TTX from controls. In these conditions, SS- V1^{R} had a significantly lower
489 g_{Nap} density (22.1 ± 12.6 pS/pF, $n = 13$) when compared to RS- V1^{R} (57.8 ± 17.4 pS/pF, $n = 7$)
490 and to PP- V1^{R} (70.6 ± 34.0 pS/pF, $n = 11$; $P < 0.0001$) (Figure 9A4). These results highlight a
491 direct relationship between the strength of I_{Nap} and the ability of V1^{R} to sustain repetitive
492 spiking and plateau potential activity.

493 To determine whether I_{NaP} is required for repetitive spiking in embryonic $V1^R$, we
494 assessed the effect of riluzole on $V1^R$ that can sustain AP firing or plateau potential activity.
495 The application of 5 μ M riluzole turned all RS- $V1^R$ into SS- $V1^R$ ($n = 10$) (Figure 9B). In the
496 presence of 5 μ M riluzole, the depolarizing current step failed to trigger more than a doublet
497 in these cells. 5 μ M riluzole did not significantly change the AP threshold (-37.2 ± 3.2 mV vs
498 -36.8 ± 6.0 mV with 5 μ M riluzole, $n = 10$, $P = 0.70$). In all PP- $V1^R$, riluzole prevented the
499 plateau potential activity ($n = 7$) (Figure 9C). Increasing the amplitude of the injected current
500 failed to evoke any AP, indicating that PP-RCs were turned into non-excitabile neurons when
501 I_{NaP} was blocked.

502 Altogether, these results indicate that I_{NaP} already plays an important role in $V1^R$
503 intrinsic activation properties at this early embryonic developmental stage of SC neuronal
504 networks.

505

506 ***Blocking persistent sodium current alters SNA pattern and SNA propagation along the***
507 ***cord.***

508 Synchronous activation of MNs and INs was proposed to drive episodes of activity
509 during SNA (Hanson and Landmesser, 2003; Czarnecki et al., 2014). If intrinsic activation
510 properties of the few INs that produce GABA including $V1^R$, rely on the I_{NaP} , we expected
511 that blocking I_{NaP} would alter episodes of activity during SNA in a manner similar to that
512 observed in the presence of GABA_AR antagonists (Hanson and Landmesser, 2003; Czarnecki
513 et al., 2014). Blocking GABA neurotransmission during SNA evoked an increase in inter-
514 episode interval, but had little effect on the duration of episode of activity and on their
515 propagation along the cord (Hanson and Landmesser, 2003). In addition, we previously
516 showed that blocking GABA neurotransmission decreased the amplitude of spontaneous giant
517 inward currents (sGICs) recorded in MNs during SNA (Czarnecki et al., 2014).

518 To determine the involvement of I_{NaP} in SNA, we first tested the effect of 5 μ M riluzole

519 on the spontaneous activity of MNs using whole-cell voltage-clamp recordings. In control
520 conditions, sGICs occurred every 4 minutes (4.0 ± 0.8 min, $n = 9$), had mean amplitude of
521 291 ± 200 pA ($n = 9$) and a half-width of 0.6 ± 0.3 s ($V_h = -60$ mV; $E_{Cl} = 3$ mV) (Figure
522 10A1-A2). The time course of the effect of riluzole on sGIC occurrence was variable among
523 MNs. In one out of nine recorded MNs, riluzole abolished GIC activity in less than 10 min. In
524 other MNs, 1 to 2 GICs could still be observed during the 20- to 30-min application of
525 riluzole. (Figure 10A2). During this transitory period, riluzole significantly reduced the
526 amplitude of GICs ($30.8 \pm 32.7\%$ reduction; $n = 8$; $P = 0.039$) (Figure 10B1) and the half-
527 duration of GICs ($44.0 \pm 27.2\%$ reduction; $n = 8$; $P = 0.0078$) (Figure 10B2). In order to assess
528 the effect of riluzole on SNA, we made long-lasting extracellular recordings of SC activity
529 using two electrodes positioned on the cervical and lumbar superficial part of the ventral horn
530 of the SC at E12.5 (Czarnecki et al., 2014) (Figure 10C1).

531 These recordings allowed us to monitor SC neuron activity related to GIC activity
532 recorded in MNs (Czarnecki et al., 2014). We found that a 30- to 40-min application of $5 \mu\text{M}$
533 riluzole significantly increased the inter-episode interval from 4.18 ± 1.93 min in control
534 conditions to 12.34 ± 9.08 min in the presence of riluzole ($P < 0.001$, $n = 12$ paired SCs)
535 ($196.3 \pm 203\%$ increase) (Figure 10C2-C3), revealing a strong involvement of the I_{Nap} current
536 in the rhythmicity of early SC network activity. We therefore analyzed individual bursts of
537 AP exhibited by the cervical (C) and lumbar (L) SC networks in the presence of riluzole. We
538 found that the duration of bursts (both C and L), compared before (2.31 ± 0.89 s) and after the
539 riluzole application (1.44 ± 0.7 s), was significantly reduced ($36.5 \pm 18.3\%$ reduction; $n = 22$;
540 $P < 0.001$) (Figure 10C4). In addition, the instantaneous AP frequency within a burst at both
541 the cervical level (C level) and the lumbar level (L level) was significantly reduced by $25.3 \pm$
542 11.9% ($P < 0.001$) in the presence of riluzole (112.4 ± 39.6 Hz in control conditions and 83.3
543 ± 34.4 Hz with riluzole, $n = 22$) (Figure 10C5). We also observed a reduction in the speed of
544 propagation of SNA episodes between the C level and L level of the SC in the presence of

545 riluzole. Propagation of SNA along the cord was investigated by analysis of the time needed
546 for a burst of AP recorded at the C level to reach L level (distance between the two recording
547 levels \approx 4mm) (Yvert et al., 2004). We found that the C-L time was significantly increased (P
548 < 0.001) from 1.56 ± 0.42 s in control conditions to 2.42 ± 0.77 s in the presence of riluzole
549 ($56.3 \pm 36.1\%$ increase; $n = 10$) (Figure 10C6).

550 Riluzole had a stronger effect on SNA than previously observed in the presence of
551 GABA_AR antagonists (Hanson and Landmesser, 2003; Czarnecki et al., 2014). Targeted
552 networks during extracellular recordings likely include MNs as well as surrounding INs
553 (Hanson and Landmesser, 2003; Czarnecki et al., 2014) including V1^R GABAergic INs.
554 Because most GABAergic V1^R are able to generate repetitive firing in response to GDP,
555 which is not the case for MNs (Czarnecki et al., 2014), this apparent discrepancy could be
556 explained if blocking GABA neurotransmission does not strongly alter GABAergic INs
557 firing, just as riluzole does. We cannot, however, exclude that I_{Nap} is also present in neurons
558 other than V1^R in the SC at E12.5. Anyhow, these results indicate that I_{Nap} plays an important
559 role in SNA at the onset of synaptogenesis (E12.5) by regulating neuron excitability in the
560 mouse embryonic SC.

561 **DISCUSSION**

562 How excitability of neurons evolves during SC development was extensively studied at
563 developmental stages at which central pattern generators are already functional. At these
564 developmental stages (P0 to P5, postnatal day), I_{Nap} is present in MNs and in SC INs (Tazerart
565 et al., 2007; Zhong et al., 2007) and is required to generate fictive locomotion (Zhong et al.,
566 2007). Here, we show that $V1^R$ already express I_{Nap} at the onset of synaptogenesis in the
567 embryonic (E12.5) SC (Scain et al., 2010). Our results reveal that I_{Nap} already closely controls
568 the $V1^R$ excitability pattern. In addition, we found that low concentrations of riluzole, an I_{Nap}
569 blocker, dramatically altered the SC SNA pattern, suggesting that I_{Nap} is already expressed by
570 neurons in the mammalian embryonic SC well before the control of muscle contraction by
571 MNs (Sanes and Lichtman, 1999).

572

573 ***$V1^R$ display different excitability patterns at the onset of SNA.***

574 Repetitive firing of presynaptic neurons is required for long-lasting neurotransmitter-
575 dependent episodes, as GDPs observed in MNs at E12.5. Previous studies have examined the
576 development of passive and active membrane properties of MNs and INs in late embryonic
577 and newborn rats or mice (Ziskind-Conhaim, 1988; Gao and Ziskind-Conhaim, 1998; Vinay
578 et al., 2000; Theiss et al., 2007; Perry et al., 2015; Bikoff et al., 2016), but there is no
579 information about the excitability of INs at early mammalian embryonic developmental stages
580 when SNA first arises. We found that a majority of $V1^R$ ($\approx 60\%$) can already generate
581 repetitive AP firing or long-lasting sodium-dependent plateau potentials at the onset of SNA,
582 indicating that these cells are already active at this early embryonic developmental stage. Our
583 analysis revealed a strong heterogeneity in $V1^R$ excitability pattern, which can be separated
584 into different independent classes, but such functional diversity is unlikely to persist in the
585 adult. In the adult, $V1^R$ were found to generate two different excitability patterns only, a
586 prominent low-threshold depolarization and burst firing followed by continuous firing

587 dependent on V_h (Perry et al., 2015; Bikoff et al., 2016). It is therefore likely that the
588 functional heterogeneity we observed at E12.5 reflects an immature form of $V1^R$ excitability
589 (Perry et al., 2015; Bikoff et al., 2016). Sodium-dependent plateau potentials were also
590 observed in ipsilateral caudal SC INs of zebrafish embryos at the appearance of functional
591 neuromuscular junctions and then disappeared at more mature stages (Tong and McDermid,
592 2012).

593

594 ***I_{Nap} already regulate excitability patterns of $V1^R$ at early developmental stages.***

595 In this study, we reveal the presence of I_{Nap} in neurons of mammalian embryos at the
596 onset of SNA. Persistent inward currents (PICs) are present in many types of neurons. PICs
597 can be calcium- and/or sodium-dependent depending on the neuron subtypes. We did not find
598 any evidence for a significant calcium component in recorded PICs in $V1^R$ at E12.5. Indeed,
599 the PIC was fully blocked by TTX in $V1^R$, which contrasts with what is known about more
600 mature spinal neurons like MNs (Hounsgaard and Kiehn, 1989; Bui et al., 2006; Carlin et al.,
601 2009). Accordingly, we concluded that immature $V1^R$ at the onset of SNA generate a pure
602 sodium-dependent PIC. I_{Nap} recorded in $V1^R$ of the mouse embryo has an activation onset (\approx -
603 65 mV) similar to that of I_{Nap} at postnatal developmental stages in the rat and mouse SC (Kuo
604 et al., 2006; Tazerart et al., 2007; Theiss et al., 2007; Tazerart et al., 2008; Dai and Jordan,
605 2010). The Boltzmann constant of activation calculated for I_{Nap} in $V1^R$ (\approx 7 mV) is in the
606 range of the values known for I_{Nap} in INs and MNs (\approx 6 mV) of neonatal rats (Bouhadfane et
607 al., 2013) or in the calyx of Held (\approx 8 mV) (Huang and Trussell, 2008). Small differences in
608 the voltage dependency of I_{Nap} activation may reflect differences in sodium channel α -subunit
609 and/or β -subunit combination expression (Isom et al., 1994; Qu et al., 2001).

610 I_{Nap} likely has diverse functions and plays an important function in locomotor pattern
611 generation in neonatal rats (Tazerart, S., *et al.* 2007). In neonate SC, I_{Nap} is present in both
612 INs and MNs (Kuo et al., 2006; Tazerart et al., 2007) and is known to generate pacemaker

613 activities in central pattern generator INs (Tazerart et al., 2008). Remarkably, I_{Nap} also
614 contributes to lumbar MN activity related to plateau potential in rat neonates (Bouhadfane et
615 al., 2013). However, while in neonate MNs, I_{Nap} is essential for self-sustained firing only
616 during calcium-dependent plateau potential depolarization (Carlin et al., 2009; Bouhadfane et
617 al., 2013), plateau potential activity in $V1^R$ at E12.5 is fully I_{Nap} -dependent

618

619 ***Does I_{Nap} already participate in SC activity at the onset of neuronal network formation?***

620 I_{Nap} plays a crucial role in the regulation of locomotor pattern generation in rat
621 neonates (Tazerart et al., 2007; Zhong et al., 2007; Bouhadfane et al., 2013) and in the SC of
622 the zebrafish embryo during the cooling stage (Tong and McDearmid, 2012). Here, we
623 demonstrated that a low concentration of riluzole dramatically reduced the amplitude and the
624 duration of GICs recorded on MNs and strongly altered SC activity (extracellular recordings)
625 at the onset of SNA.

626 In our experiments, we used a concentration of riluzole that has a minimal effect on the
627 sodium AP waveform (Figure 6). However, beside its effect on I_{Nap} , riluzole is known to
628 inhibit the release of glutamate (Cheramy et al., 1992), to inhibit AMPA receptor activation
629 (Albo et al., 2004), GABA_A and glycine receptor activation (Mohammadi et al., 2001) and to
630 block several voltage-gated channels including calcium channels (Huang et al., 1997; Ahn et
631 al., 2006). With the exception of AMPA receptor inhibition (Albo et al., 2004), these side
632 effects of riluzole occur at concentrations $\geq 10 \mu\text{M}$ (Cheramy et al., 1992; Huang et al., 1997;
633 Mohammadi et al., 2001; Ahn et al., 2006). Because the inhibition of glutamate
634 neurotransmission did not alter SNA in the mouse embryonic SC at E12.5 (Czarnecki et al.,
635 2014), it is unlikely that the alteration of SNA we observed in the presence of $5 \mu\text{M}$ riluzole is
636 caused by the inhibition of glutamatergic synaptic activity (Albo et al., 2004). Accordingly,
637 we propose that I_{Nap} already regulates the SNA pattern at the onset of synaptogenesis in
638 mammalian embryos before the formation of the locomotor SC network and of functional

639 neuromuscular junctions. However, we cannot exclude that spinal neurons other than $V1^R$
640 exhibit I_{Nap} -dependent sustain discharge at this developmental stage.

641 Because $V1^R$ already produce GABA at E12.5 and make synaptic-like contacts with
642 MNs while MNs make synaptic-like contacts with $V1^R$ (see also (Alvarez et al., 2013), it is
643 likely that $V1^R$ participate in early SC SNA. Although correlative, our data reinforce the
644 hypothesis that a primitive $V1^R$ -MN recurrent-like circuit may exist at the onset of
645 synaptogenesis in the mouse embryo. This primitive $V1^R$ -MN recurrent circuit differs in
646 several ways from the adult RC-MN recurrent circuits. Evoked MN spiking did not trigger a
647 recurrent synaptic response at E12.5 (Le Bras et al., 2014), which suggests that although $V1^R$
648 projects on MNs and vice versa, it is unlikely that $V1^R$ projecting on MNs receive inputs from
649 these MNs and vice versa. It is also unlikely that MN release sites apposed on $V1^R$ are mixed
650 glutamatergic and cholinergic inputs as observed at postnatal stages (Nishimaru et al., 2005;
651 Lamotte d'Incamps et al., 2017). Glutamatergic vesicular transporters were not observed
652 within MNs at E12.5 (Czarnecki et al., 2014). But we cannot completely exclude that some
653 immature motor axon synapses on $V1^R$ already release aspartate, as suggested in the adult
654 (Richards et al., 2014). However, contrary to what is observed for GABAergic and
655 cholinergic networks, the spontaneous activation of glutamate receptors had a minor role only
656 in the generation of SNA episodes at E12.5 (Czarnecki et al., 2014).

657 We clearly show that paracrine release of GABA can occur in the embryonic SC, which
658 may explain the smooth shape of GABAergic-dependent GDPs observed in MNs during SNA
659 (Czarnecki et al., 2014). Since $V1^R$ are GABAergic at this embryonic age and possess
660 putative release sites, $V1^R$ may be one of the sources for the paracrine release of GABA we
661 observed. Accordingly, we propose that $V1^R$ -MN interactions occur through synaptic and
662 paracrine release and participate in the synchronization of neuronal assembly required for the
663 generation of the propagating waves of activity characterizing SC SNA at E12.5 (Momose-
664 Sato and Sato, 2013).

665

666 ***Conclusions***

667 Taken together, our findings demonstrate that I_{Nap} is already present in developing SC
668 neurons at an early developmental stage and governs $V1^R$ excitability. I_{Nap} plays an important
669 role in the regulation of locomotor pattern generation at postnatal developmental stages in
670 rodents (Tazerart et al., 2008). Because the application of a low concentration of riluzole
671 altered SNA, we propose that I_{Nap} contributes to the patterning of embryonic SC activity at the
672 onset of synaptogenesis. Accordingly, the capacity of SC neurons to generate sustained firing
673 must be crucial for correct embryonic SC patterned activity at the onset of synaptogenesis,
674 which is required for the correct development of MN projections toward their peripheral
675 targets (Hanson and Landmesser, 2006).

676

677 **BIBLIOGRAPHY**

- 678 Ahn HS, Kim SE, Jang HJ, Kim MJ, Rhie DJ, Yoon SH, Jo YH, Kim MS, Sung KW, Hahn
679 SJ (2006) Interaction of riluzole with the closed inactivated state of Kv4.3 channels.
680 *The Journal of pharmacology and experimental therapeutics* 319:323-331.
- 681 Albo F, Pieri M, Zona C (2004) Modulation of AMPA receptors in spinal motor neurons by
682 the neuroprotective agent riluzole. *Journal of neuroscience research* 78:200-207.
- 683 Allain AE, Bairi A, Meyrand P, Branchereau P (2004) Ontogenic changes of the GABAergic
684 system in the embryonic mouse spinal cord. *Brain research* 1000:134-147.
- 685 Allain AE, Bairi A, Meyrand P, Branchereau P (2006) Expression of the glycinergic system
686 during the course of embryonic development in the mouse spinal cord and its co-
687 localization with GABA immunoreactivity. *The Journal of comparative neurology*
688 496:832-846.
- 689 Alvarez FJ, Benito-Gonzalez A, Siembab VC (2013) Principles of interneuron development
690 learned from Renshaw cells and the motoneuron recurrent inhibitory circuit. *Annals of*
691 *the New York Academy of Sciences* 1279:22-31.
- 692 Barberis A, Mozrzymas JW, Ortinski PI, Vicini S (2007) Desensitization and binding
693 properties determine distinct $\alpha 1\beta 2\gamma 2$ and $\alpha 3\beta 2\gamma 2$ GABA(A)
694 receptor-channel kinetic behavior. *The European journal of neuroscience* 25:2726-
695 2740.
- 696 Ben-Ari Y, Cherubini E, Corradetti R, Gaiarsa JL (1989) Giant synaptic potentials in
697 immature rat CA3 hippocampal neurones. *J Physiol* 416:303-325.
- 698 Benito-Gonzalez A, Alvarez FJ (2012) Renshaw cells and Ia inhibitory interneurons are
699 generated at different times from p1 progenitors and differentiate shortly after exiting
700 the cell cycle. *J Neurosci* 32:1156-1170.
- 701 Bikoff JB, Gabitto MI, Rivard AF, Drobac E, Machado TA, Miri A, Brenner-Morton S,
702 Famojure E, Diaz C, Alvarez FJ, Mentis GZ, Jessell TM (2016) Spinal Inhibitory
703 Interneuron Diversity Delineates Variant Motor Microcircuits. *Cell* 165:207-219.
- 704 Bouhadfane M, Tazerart S, Moqrish A, Vinay L, Brocard F (2013) Sodium-mediated plateau
705 potentials in lumbar motoneurons of neonatal rats. *J Neurosci* 33:15626-15641.
- 706 Bui TV, Ter-Mikaelian M, Bedrossian D, Rose PK (2006) Computational estimation of the
707 distribution of L-type Ca(2+) channels in motoneurons based on variable threshold of
708 activation of persistent inward currents. *Journal of neurophysiology* 95:225-241.
- 709 Carlin KP, Bui TV, Dai Y, Brownstone RM (2009) Staircase currents in motoneurons: insight
710 into the spatial arrangement of calcium channels in the dendritic tree. *J Neurosci*
711 29:5343-5353.
- 712 Carr PA, Alvarez FJ, Leman EA, Fyffe RE (1998) Calbindin D28k expression in
713 immunohistochemically identified Renshaw cells. *Neuroreport* 9:2657-2661.
- 714 Cheramy A, Barbeito L, Godeheu G, Glowinski J (1992) Riluzole inhibits the release of
715 glutamate in the caudate nucleus of the cat in vivo. *Neuroscience letters* 147:209-212.
- 716 Corlew R, Bosma MM, Moody WJ (2004) Spontaneous, synchronous electrical activity in
717 neonatal mouse cortical neurones. *J Physiol* 560:377-390.
- 718 Czarnecki A, Le Corrionc H, Rigato C, Le Bras B, Couraud F, Scain AL, Allain AE, Mouffle
719 C, Bullier E, Mangin JM, Branchereau P, Legendre P (2014) Acetylcholine controls
720 GABA-, glutamate-, and glycine-dependent giant depolarizing potentials that govern
721 spontaneous motoneuron activity at the onset of synaptogenesis in the mouse
722 embryonic spinal cord. *J Neurosci* 34:6389-6404.
- 723 Dai Y, Jordan LM (2010) Multiple patterns and components of persistent inward current with
724 serotonergic modulation in locomotor activity-related neurons in Cfos-EGFP mice.
725 *Journal of neurophysiology* 103:1712-1727.

- 726 Delpy A, Allain AE, Meyrand P, Branchereau P (2008) NKCC1 cotransporter inactivation
727 underlies embryonic development of chloride-mediated inhibition in mouse spinal
728 motoneuron. *J Physiol* 586:1059-1075.
- 729 Dottori M, Gross MK, Labosky P, Goulding M (2001) The winged-helix transcription factor
730 *Foxd3* suppresses interneuron differentiation and promotes neural crest cell fate.
731 *Development* 128:4127-4138.
- 732 Eccles JC, Fatt P, Landgren S (1956) The inhibitory pathway to motoneurons. *Progress in*
733 *neurobiology*:72-82.
- 734 Feller MB (1999) Spontaneous correlated activity in developing neural circuits. *Neuron*
735 22:653-656.
- 736 Gao BX, Ziskind-Conhaim L (1998) Development of ionic currents underlying changes in
737 action potential waveforms in rat spinal motoneurons. *Journal of neurophysiology*
738 80:3047-3061.
- 739 Garaschuk O, Hanse E, Konnerth A (1998) Developmental profile and synaptic origin of
740 early network oscillations in the CA1 region of rat neonatal hippocampus. *J Physiol*
741 507 (Pt 1):219-236.
- 742 Garaschuk O, Linn J, Eilers J, Konnerth A (2000) Large-scale oscillatory calcium waves in
743 the immature cortex. *Nat Neurosci* 3:452-459.
- 744 Geiman EJ, Knox MC, Alvarez FJ (2000) Postnatal maturation of gephyrin/glycine receptor
745 clusters on developing Renshaw cells. *The Journal of comparative neurology* 426:130-
746 142.
- 747 Gonzalez-Islas C, Wenner P (2006) Spontaneous network activity in the embryonic spinal
748 cord regulates AMPAergic and GABAergic synaptic strength. *Neuron* 49:563-575.
- 749 Gust J, Wright JJ, Pratt EB, Bosma MM (2003) Development of synchronized activity of
750 cranial motor neurons in the segmented embryonic mouse hindbrain. *J Physiol*
751 550:123-133.
- 752 Hanson MG, Landmesser LT (2003) Characterization of the circuits that generate
753 spontaneous episodes of activity in the early embryonic mouse spinal cord. *J Neurosci*
754 23:587-600.
- 755 Hanson MG, Landmesser LT (2006) Increasing the frequency of spontaneous rhythmic
756 activity disrupts pool-specific axon fasciculation and pathfinding of embryonic spinal
757 motoneurons. *J Neurosci* 26:12769-12780.
- 758 Hanson MG, Milner LD, Landmesser LT (2008) Spontaneous rhythmic activity in early chick
759 spinal cord influences distinct motor axon pathfinding decisions. *Brain Res Rev*
760 57:77-85.
- 761 Hounsgaard J, Kiehn O (1989) Serotonin-induced bistability of turtle motoneurons caused by
762 a nifedipine-sensitive calcium plateau potential. *J Physiol* 414:265-282.
- 763 Huang CS, Song JH, Nagata K, Yeh JZ, Narahashi T (1997) Effects of the neuroprotective
764 agent riluzole on the high voltage-activated calcium channels of rat dorsal root
765 ganglion neurons. *The Journal of pharmacology and experimental therapeutics*
766 282:1280-1290.
- 767 Huang H, Trussell LO (2008) Control of presynaptic function by a persistent Na(+) current.
768 *Neuron* 60:975-979.
- 769 Isom LL, De Jongh KS, Catterall WA (1994) Auxiliary subunits of voltage-gated ion
770 channels. *Neuron* 12:1183-1194.
- 771 Kirkby LA, Sack GS, Firl A, Feller MB (2013) A role for correlated spontaneous activity in
772 the assembly of neural circuits. *Neuron* 80:1129-1144.
- 773 Kuo JJ, Lee RH, Zhang L, Heckman CJ (2006) Essential role of the persistent sodium current
774 in spike initiation during slowly rising inputs in mouse spinal neurones. *J Physiol*
775 574:819-834.

- 776 Lamotte d'Incamps B, Bhumbra GS, Foster JD, Beato M, Ascher P (2017) Segregation of
777 glutamatergic and cholinergic transmission at the mixed motoneuron Renshaw cell
778 synapse. *Scientific reports* 7:4037.
- 779 Landmesser LT, O'Donovan MJ (1984) Activation patterns of embryonic chick hind limb
780 muscles recorded in ovo and in an isolated spinal cord preparation. *J Physiol* 347:189-
781 204.
- 782 Le Bras B, Freal A, Czarnecki A, Legendre P, Bullier E, Komada M, Brophy PJ, Davenne M,
783 Couraud F (2014) In vivo assembly of the axon initial segment in motor neurons.
784 *Brain structure & function* 219:1433-1450.
- 785 Le-Corronc H, Rigo JM, Branchereau P, Legendre P (2011) GABA(A) receptor and glycine
786 receptor activation by paracrine/autocrine release of endogenous agonists: more than a
787 simple communication pathway. *Molecular neurobiology* 44:28-52.
- 788 Lee RH, Heckman CJ (1998) Bistability in spinal motoneurons in vivo: systematic variations
789 in persistent inward currents. *Journal of neurophysiology* 80:583-593.
- 790 Marder E, Rehm KJ (2005) Development of central pattern generating circuits. *Curr Opin*
791 *Neurobiol* 15:86-93.
- 792 Mohammadi B, Krampfl K, Moschref H, Dengler R, Bufler J (2001) Interaction of the
793 neuroprotective drug riluzole with GABA(A) and glycine receptor channels. *European*
794 *journal of pharmacology* 415:135-140.
- 795 Momose-Sato Y, Sato K (2013) Optical imaging of the spontaneous depolarization wave in
796 the mouse embryo: origins and pharmacological nature. *Annals of the New York*
797 *Academy of Sciences* 1279:60-70.
- 798 Moody WJ (1998) Control of spontaneous activity during development. *Journal of*
799 *neurobiology* 37:97-109.
- 800 Muller A, Kukley M, Stausberg P, Beck H, Muller W, Dietrich D (2005) Endogenous Ca²⁺
801 buffer concentration and Ca²⁺ microdomains in hippocampal neurons. *J Neurosci*
802 25:558-565.
- 803 Myers CP, Lewcock JW, Hanson MG, Gosgnach S, Aimone JB, Gage FH, Lee KF,
804 Landmesser LT, Pfaff SL (2005) Cholinergic input is required during embryonic
805 development to mediate proper assembly of spinal locomotor circuits. *Neuron* 46:37-
806 49.
- 807 Nishimaru H, Restrepo CE, Ryge J, Yanagawa Y, Kiehn O (2005) Mammalian motor neurons
808 corelease glutamate and acetylcholine at central synapses. *Proceedings of the National*
809 *Academy of Sciences of the United States of America* 102:5245-5249.
- 810 Perry S, Gezelius H, Larhammar M, Hilscher MM, Lamotte d'Incamps B, Leao KE,
811 Kullander K (2015) Firing properties of Renshaw cells defined by *Chrna2* are
812 modulated by hyperpolarizing and small conductance ion currents *I_h* and *ISK*. *The*
813 *European journal of neuroscience* 41:889-900.
- 814 Prasad T, Wang X, Gray PA, Weiner JA (2008) A differential developmental pattern of spinal
815 interneuron apoptosis during synaptogenesis: insights from genetic analyses of the
816 protocadherin-gamma gene cluster. *Development* 135:4153-4164.
- 817 Qu Y, Curtis R, Lawson D, Gilbride K, Ge P, DiStefano PS, Silos-Santiago I, Catterall WA,
818 Scheuer T (2001) Differential modulation of sodium channel gating and persistent
819 sodium currents by the beta1, beta2, and beta3 subunits. *Molecular and cellular*
820 *neurosciences* 18:570-580.
- 821 Richards DS, Griffith RW, Romer SH, Alvarez FJ (2014) Motor axon synapses on rensaw
822 cells contain higher levels of aspartate than glutamate. *PloS one* 9:e97240.
- 823 Rockhill W, Kirkman JL, Bosma MM (2009) Spontaneous activity in the developing mouse
824 midbrain driven by an external pacemaker. *Dev Neurobiol* 69:689-704.
- 825 Safiulina VF, Cherubini E (2009) At immature mossy fibers-CA3 connections, activation of
826 presynaptic GABA(B) receptors by endogenously released GABA contributes to
827 synapses silencing. *Frontiers in cellular neuroscience* 3:1.

- 828 Sanes JR, Lichtman JW (1999) Development of the vertebrate neuromuscular junction.
829 Annual review of neuroscience 22:389-442.
- 830 Sapir T, Geiman EJ, Wang Z, Velasquez T, Mitsui S, Yoshihara Y, Frank E, Alvarez FJ,
831 Goulding M (2004) Pax6 and engrailed 1 regulate two distinct aspects of rensaw cell
832 development. *J Neurosci* 24:1255-1264.
- 833 Scain AL, Le Corrone H, Allain AE, Muller E, Rigo JM, Meyrand P, Branchereau P,
834 Legendre P (2010) Glycine release from radial cells modulates the spontaneous
835 activity and its propagation during early spinal cord development. *J Neurosci* 30:390-
836 403.
- 837 Stam FJ, Hendricks TJ, Zhang J, Geiman EJ, Francius C, Labosky PA, Clotman F, Goulding
838 M (2012) Renshaw cell interneuron specialization is controlled by a temporally
839 restricted transcription factor program. *Development* 139:179-190.
- 840 Tamamaki N, Yanagawa Y, Tomioka R, Miyazaki J, Obata K, Kaneko T (2003) Green
841 fluorescent protein expression and colocalization with calretinin, parvalbumin, and
842 somatostatin in the GAD67-GFP knock-in mouse. *The Journal of comparative*
843 *neurology* 467:60-79.
- 844 Tazerart S, Vinay L, Brocard F (2008) The persistent sodium current generates pacemaker
845 activities in the central pattern generator for locomotion and regulates the locomotor
846 rhythm. *J Neurosci* 28:8577-8589.
- 847 Tazerart S, Viemari JC, Darbon P, Vinay L, Brocard F (2007) Contribution of persistent
848 sodium current to locomotor pattern generation in neonatal rats. *Journal of*
849 *neurophysiology* 98:613-628.
- 850 Theiss RD, Kuo JJ, Heckman CJ (2007) Persistent inward currents in rat ventral horn
851 neurones. *J Physiol* 580:507-522.
- 852 Tong H, McDearmid JR (2012) Pacemaker and plateau potentials shape output of a
853 developing locomotor network. *Current biology : CB* 22:2285-2293.
- 854 Urbani A, Belluzzi O (2000) Riluzole inhibits the persistent sodium current in mammalian
855 CNS neurons. *The European journal of neuroscience* 12:3567-3574.
- 856 Vinay L, Brocard F, Pflieger JF, Simeoni-Alias J, Clarac F (2000) Perinatal development of
857 lumbar motoneurons and their inputs in the rat. *Brain research bulletin* 53:635-647.
- 858 Watt AJ, Cuntz H, Mori M, Nusser Z, Sjöström PJ, Häusser M (2009) Traveling waves in
859 developing cerebellar cortex mediated by asymmetrical Purkinje cell connectivity. *Nat*
860 *Neurosci* 12:463-473.
- 861 Wenner P, O'Donovan MJ (2001) Mechanisms that initiate spontaneous network activity in
862 the developing chick spinal cord. *Journal of neurophysiology* 86:1481-1498.
- 863 Wichterle H, Lieberam I, Porter JA, Jessell TM (2002) Directed differentiation of embryonic
864 stem cells into motor neurons. *Cell* 110:385-397.
- 865 Young SH, Poo MM (1983) Spontaneous release of transmitter from growth cones of
866 embryonic neurones. *Nature* 305:634-637.
- 867 Yvert B, Branchereau P, Meyrand P (2004) Multiple spontaneous rhythmic activity patterns
868 generated by the embryonic mouse spinal cord occur within a specific developmental
869 time window. *Journal of neurophysiology* 91:2101-2109.
- 870 Zhang LI, Poo MM (2001) Electrical activity and development of neural circuits. *Nat*
871 *Neurosci* 4 Suppl:1207-1214.
- 872 Zhong G, Masino MA, Harris-Warrick RM (2007) Persistent sodium currents participate in
873 fictive locomotion generation in neonatal mouse spinal cord. *J Neurosci* 27:4507-
874 4518.
- 875 Ziskind-Conhaim L (1988) Electrical properties of motoneurons in the spinal cord of rat
876 embryos. *Developmental biology* 128:21-29.
- 877 Ziskind-Conhaim L, Wu L, Wiesner EP (2008) Persistent sodium current contributes to
878 induced voltage oscillations in locomotor-related hb9 interneurons in the mouse spinal
879 cord. *Journal of neurophysiology* 100:2254-2264.

880

881 **LEGENDS**882 ***Figure 1: VI^R identification in the lumbar spinal cord of E12.5 embryos***

883 A) Coronal slice of the lumbar spinal cord of E12.5 GA67-eGFP mouse embryo showing the
884 distribution of eGFP neurons (A1), FoxD3 (A2) and calbindin (A3) immunoreactive neurons.

885 A4) Superimposed images showing the colocalization of eGFP, FoxD3 immunostaining and
886 calbindin immunostaining. B) Enlarged images from A showing that eGFP neurons localized

887 in the ventrolateral area of the spinal cord (B1) are Foxd3 immunoreactive (B2), most of them
888 being calbindin immunoreactive (B3-B4). C) Coronal slice of the ventrolateral part of the

889 lumbar spinal cord of E12.5 GA67-eGFP mouse embryo showing the distribution of eGFP
890 neurons (C1), FoxD3 (C2) and MafB (C3) immunoreactive neurons. C4) Superimposed

891 images showing the colocalization of eGFP FoxD3 immunostaining and MafB
892 immunostaining. Note that all FoxD3 immunoreactive neurons localized in the marginal zone

893 of the ventrolateral area are also MafB-positive, indicating that they are VI^R neurons. D1)
894 Example of a neuron filled with neurobiotin during the recording at the lumbar level of an

895 embryonic spinal cord open book preparation of GAD67-GFP mice at E12.5. This eGFP
896 neuron (D2) was immunoreactive to Foxd3 antibody (D3), as shown in the merged images

897 (D4). Each image corresponds to a single confocal section.

898

899 ***Figure 2: VI^R already produce GABA in the lumbar spinal cord of E12.5 embryos***

900 A) Single confocal sections of coronal slice of the lumbar spinal cord of E12.5 GA67-eGFP
901 mouse embryo showing the distribution of eGFP neurons (A1), calbindin (A2) and GABA

902 (A3) immunoreactive neurons. A4) Superimposed images showing the colocalization of
903 eGFP, calbindin immunostaining and GABA immunostaining. B1-B3) Enlarged images from

904 A1, A2 and A3 showing eGFP neurons (B1), calbindin immunoreactive neurons (B2), and
905 GABA immunoreactive neurons (B3) in the ventrolateral area of the spinal cord. B4)

906 Superimposed images showing the colocalization of calbindin immunostaining and GABA

907 immunostaining with z projections within a stack. Note the colocalization of calbindin
908 immunostaining and GABA immunostaining in the three axes, indicating that $V1^R$ already
909 produce GABA at E12.5.

910

911 ***Figure 3: $V1^R$ make synaptic-like contacts with motoneurons (HB9-eGFP) at E12.5.***

912 A) Coronal slice of the lumbar spinal cord of E12.5 HB9-eGFP mouse embryo with cell
913 nucleus staining (Hoesch) and synaptophysin immunostaining (A1). A1) Note that
914 synaptophysin immunostaining is mainly restricted in the ventral funiculus (VF) A2)
915 Calbindin staining showing the distribution of $V1^R$ neurite extensions and synaptophysin
916 immunostaining. A3) eGFP immunostaining showing the distribution of MN neurite
917 extensions and synaptophysin immunostaining. Antibody against GFP was used to visualize
918 MN morphology better (Czarnecki et al., 2014). A4) Superimposition of eGFP fluorescence,
919 calbindin immunostaining and synaptophysin immunostaining (A1, A2, A3, and A4 are
920 confocal stacks). B) Single confocal sections with z projections of enlarged images from A2,
921 A3 and A4 showing the colocalization of synaptophysin punctates with calbindin
922 immunostaining apposed to eGFP immunostaining (B1, B2 and B3; enlarged images in
923 boxes). B2) Note that a synaptophysin punctate colocalized with calbindin immunostaining
924 (B1, arrow) did not colocalize with eGFP immunostaining (B2, arrow). Note that
925 synaptophysin punctate colocalized with eGFP immunostaining (B1, arrow heads) did not
926 colocalize with calbindin immunostaining (B2, arrow head). Barred arrow (B1) shows a
927 colocalization of calbindin and synaptophysin immunostaining not apposed to eGFP
928 immunostaining. B4) superimposed images (B1, B2 and B3) with z projections showing
929 calbindin immunostaining and eGFP appositions. C1) Confocal stacks showing neurobiotin
930 injected Foxd3 immunoreactive $V1^R$, HB9-eGFP immunostaining and synaptophysin
931 immunostaining in an SC open book preparation. C2-C4). Single confocal sections with z
932 projections of enlarged images from C1 (white box) showing the colocalization of

933 synaptophysin punctates with neurobiotin staining (C2), the apposition of the same
934 synaptophysin punctates to eGFP (C3) and the apposition of neurobiotin staining containing
935 synaptophysin punctates to eGFP (C4) (enlarged image in boxes in C2, C3 and C4),
936 indicating the presence of a V1^R synaptic-like contact on an MN neurite.

937

938 ***Figure 4: Paracrine release of GABA detected by a sniffer outside-out patch.***

939 A1) Upper drawing showing the location of the outside-out sniffer to detect paracrine release
940 of GABA (left) and to obtain outside-out currents in response to GABA application (left).

941 Lower traces (purple): example of outside-out sniffer current evoked by the application of 30
942 mM KCl when the sniffer electrode was positioned in the dorsal area of the SC close to motor
943 columns. Enlarged trace shows single channel currents at the onset of the sniffer current.

944 Right traces (green) show outside-out current evoked by the application of 3 μ M and 10 μ M
945 GABA to a sniffer patch positioned outside the spinal cord. Purple and green traces are from
946 the same outside-out patch. A2) Box plots of normalized maximum outside-out current

947 evoked by KCl application (purple left) and by the application of 3 μ M or 10 μ M GABA
948 (green right) on the same outside-out sniffer patch (n = 9). Amplitudes of the outside-out
949 currents evoked by the application of 30 mM KCl, 3 μ M or 10 μ M GABA, were normalized

950 to the amplitude of the outside-out currents evoked by the application of 30 μ M GABA (not
951 shown). Note that the normalized amplitude of the outside-out current evoked by 30 mM KCl
952 application (0.118 ± 0.097) was not significantly different ($P > 0.9$) from the normalized

953 amplitude of the outside-out current evoked by the application of 3 μ M GABA ($0.152 \pm$
954 0.062). Normalized amplitudes of the outside-out currents evoked by the application of 30
955 mM KCl or of 3 μ M GABA were significantly different (KCl: $P = 0.0029$; 3 μ M GABA: $P =$

956 0.00665) from the normalized amplitude of the outside-out currents evoked by the application
957 of 10 μ M GABA (0.697 ± 0.073). V1^R: immature Renshaw cell; MN: motoneuron; ** $P <$
958 0.01 . B1) Example of motoneuron membrane potential depolarization evoked by the

959 application of 3 μM GABA in the presence of 1 μM TTX (current clamp recording: $V_h = -60$
960 mV; $E_{\text{Cl}} = -30$ mV). The application of 3 μM GABA evoked a depolarizing response of 20.6
961 ± 6.1 mV ($n = 7$).

962

963 **Figure 5: $V1^{\text{R}}$ display plateau potential, repetitive firing or generate a single action**
964 **potential during episodes of SNA in E12.5 spinal cord.**

965 Examples of spontaneous activities recorded in $V1^{\text{R}}$ being characterized by GDPs displaying
966 plateau potential (A), repetitive firing (B) or a single action potential (C) activity (V holding =
967 -60 mV). Recordings shown in A, B and C are from different cells.

968

969 **Figure 6: $V1^{\text{R}}$ display different excitability patterns in E12.5 embryonic spinal cords.**

970 Excitability patterns were analyzed using depolarizing current step (2 sec) and depolarizing
971 current ramp (20 sec). A-D) Representative traces of voltage responses showing single-
972 spiking activity (A), plateau potential activity (B) repetitive AP firing (C) and mixed
973 repetitive-spiking/plateau potential activity (D). E) Proportions of $V1^{\text{R}}$ subtypes according to
974 the observed discharge patterns. 28.6% of $V1^{\text{R}}$ could not sustain repetitive spiking, 41.7%
975 were repetitive-spiking $V1^{\text{R}}$, 8.5% were mixed $V1^{\text{R}}$, 21.2% were plateau potential $V1^{\text{R}}$ ($n =$
976 164). F) Plateau potentials are blocked by TTX (1 μM) application ($n = 5/5$) (F1, F2). F2)
977 Plateau potentials are evoked by short (100 ms) pulses of depolarizing current.

978

979 **Figure 7: Persistent sodium current (I_{Nap}) is already expressed in $V1^{\text{R}}$**

980 A1) Representative trace of I_{Nap} evoked by a slow depolarizing voltage ramp in a $V1^{\text{R}}$ (CsCl
981 intracellular solution). I_{Nap} (black trace) was isolated by subtracting the current elicited by a
982 voltage ramp (70 mV/s) in the presence of TTX (insert green trace) from the control current
983 (insert black trace). TTX-sensitive current was blocked by 5 μM riluzole (red trace). Left
984 insert shows the protocol to generate voltage-dependent slow inward currents in control

985 conditions (black), after 5 μM riluzole application (red) or 1 μM TTX application (green).
 986 Right insert shows the current evoked by a depolarizing voltage step from -100 mV to 20 mV
 987 in the absence and in the presence of 5 μM riluzole. A2) Voltage dependence of I_{Nap}
 988 conductance calculated from the trace shown in A1. The activation curve was obtained by
 989 transforming the current evoked by a depolarizing voltage ramp from -100 mV to 20 mV (70
 990 mV/s) using the following equation: $G_{\text{Nap}} = -I_{\text{Nap}}/((-V_h)+E_{\text{Na}^+})$ where V_h is the holding
 991 potential at time t during a depolarizing voltage ramp and E_{Na^+} is the equilibrium potential for
 992 sodium ($E_{\text{Na}^+} = 60$ mV). The G_{Nap}/V_h curve was fitted with a Boltzmann function (see
 993 methods), where V_{half} is the V_h value for I_{Nap} half activation, k the slope factor of the curve
 994 and G_{max} the maximum conductance. B) Box plot showing G_{max} density in RCs ($n=12$). C)
 995 Box plots showing the variation of the % I_{Nap} block by 5 μM riluzole in RC.

996

997 ***Figure 8: Effect of 5 and 10 μM riluzole on action potentials.***

998 A) Effect of 5 μM (red trace) and 10 μM (blue trace) riluzole on the action potential (AP)
 999 evoked by a depolarizing current step in an MN. B1) Box plot showing the % changes in AP
 1000 amplitude (% of control) in the presence of 5 μM riluzole and 10 μM riluzole. B2) Box plot
 1001 showing the % changes in AP threshold (% of control) in the presence of 5 μM and 10 μM
 1002 riluzole. B3) Box plot showing the % changes in AP half-width (% of control) in the presence
 1003 of 5 μM and 10 μM riluzole.

1004

1005 ***Figure 9: Sustained discharge in embryonic $V1^{\text{R}}$ depends on persistent sodium current***
 1006 ***(I_{Nap}).***

1007 A) Representative traces of I_{Nap} recorded in $V1^{\text{R}}$ that cannot sustain repetitive spiking (SS-
 1008 $V1^{\text{R}}$) (A1), in a repetitive-spiking $V1^{\text{R}}$ (RS- $V1^{\text{R}}$) (A2) and in a plateau potential $V1^{\text{R}}$ (PP-
 1009 $V1^{\text{R}}$) (A3). I_{Nap} was isolated by subtracting the current elicited by a slow voltage ramp (-100
 1010 to + 20 mV; 70 mV/s) in the presence of 1 μM TTX from the current evoked in the absence of

1011 TTX. A4) Box plots showing Gmax density in SS-V1^R (n=13), RS-RCs (n=8) and PP-V1^R (n
1012 = 11). Note that Gmax density is significantly lower in SS-V1^R (p <0.01). B) Representative
1013 traces showing the effect of riluzole application (5 μ M) on the intrinsic activity pattern
1014 evoked by suprathreshold current steps (left traces) or a suprathreshold current ramp (right
1015 traces) in an RS-V1^R. Note that riluzole blocks repetitive spiking (n= 10/10). C)
1016 Representative traces showing the effect of riluzole application on plateau potential evoked by
1017 suprathreshold current steps (left traces) or by a suprathreshold current ramp (right traces) in a
1018 V1^R. Note that riluzole blocks plateau potential activity (n=7/7).

1019

1020 ***Figure 10: Riluzole dramatically decreases the frequency and duration of episodes of SNA***
1021 ***in E12.5 embryonic spinal cord.***

1022 A1) Application of 5 μ M riluzole inhibits spontaneous giant inward current (GIC) activity in
1023 MNs (voltage clamp recordings; V_h = -60 mV; ECl = -30 mV). A2) Enlarged trace from (A1)
1024 showing GIC before (1, black) and at the onset of riluzole application (2, red). Note that the
1025 amplitude and the duration of GICs were decreased on riluzole application. B1: Box plots
1026 showing the amplitude of the GIC in a control and on riluzole application (n=8). B2: Box
1027 plots showing half amplitude durations of the GIC in control and on riluzole application
1028 (n=8). Note that the amplitude (P < 0.05) and the duration (P < 0.01) of GICs were
1029 significantly reduced in the presence of riluzole. C) Spontaneous network activity (SNA)
1030 recorded at the cervical (C) and lumbar (L) levels (see schematic drawing on the left) in
1031 extracellular configuration before (C1) and after 5 μ M riluzole (C2). Note that one episode
1032 still occurred 35 minutes after riluzole application. C3-C6) Box plots illustrating inter-burst
1033 interval, burst duration, intra-burst spike frequency and cervical-lumbar delay of episode
1034 propagation.

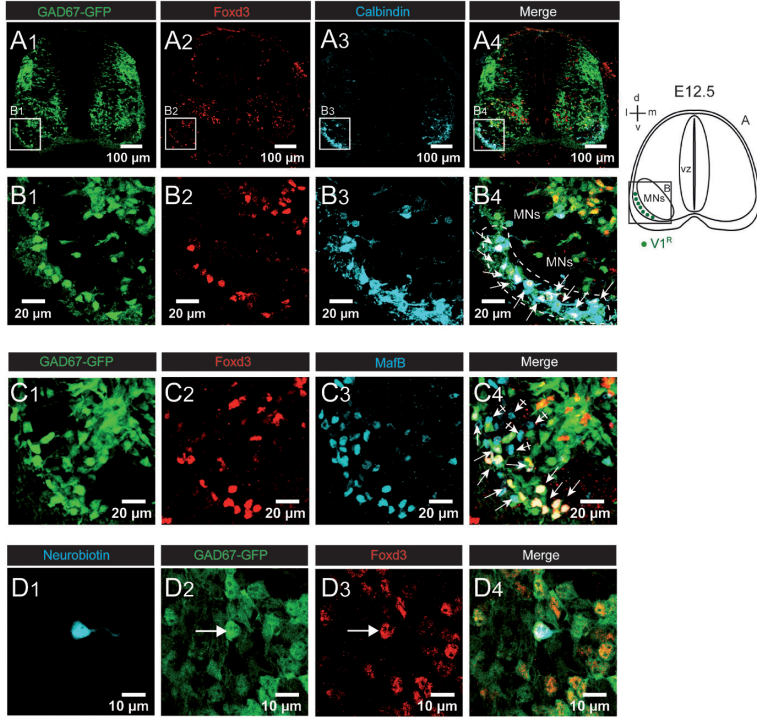
1035

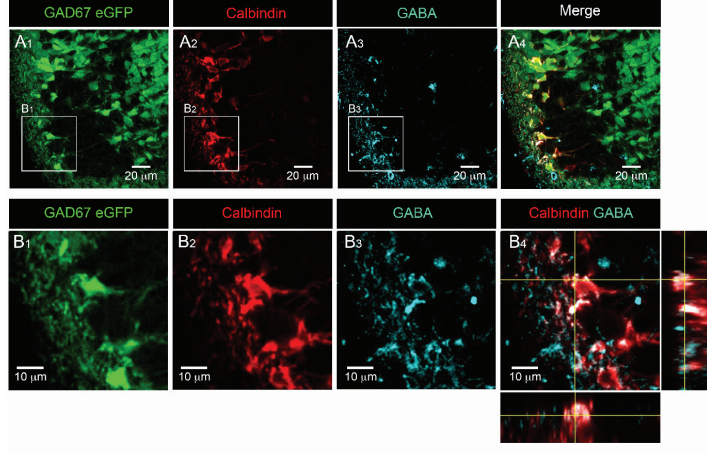
1036 **Table 1 Primary antibodies.**

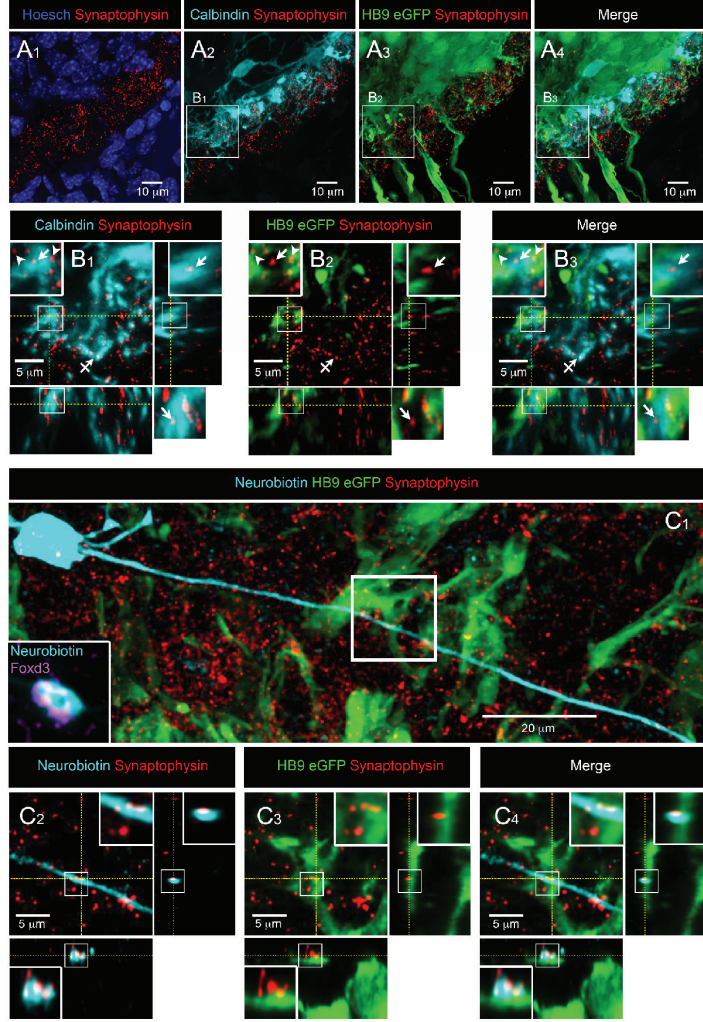
1037

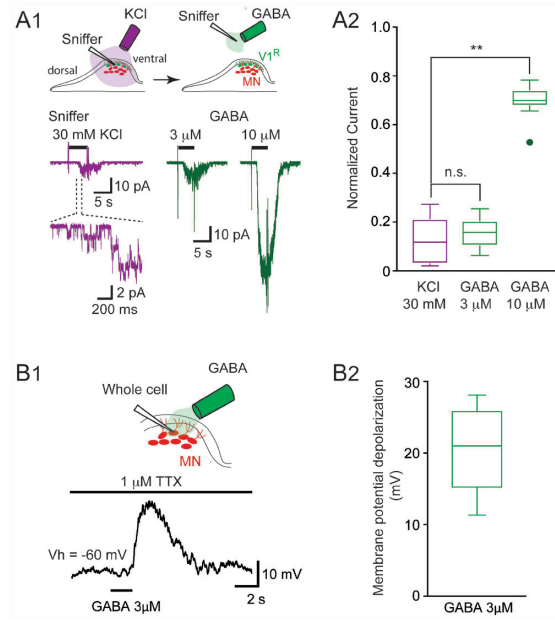
1038 **Table 2: Intrinsic membrane properties of Renshaw cells.**

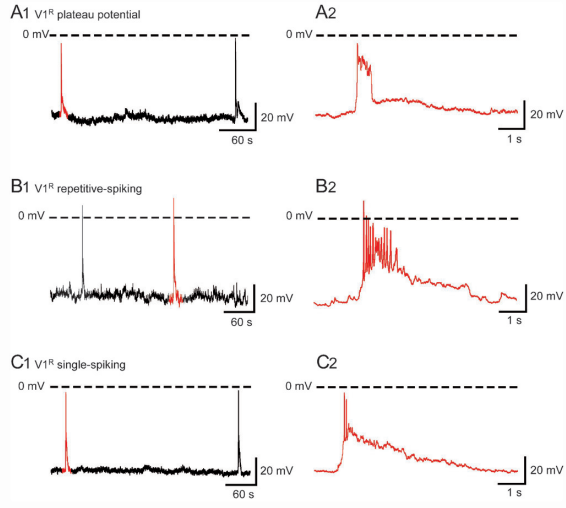
1039 SS-V1^R: single-spiking Renshaw cells, RS-V1^R: repetitive-spiking Renshaw cells, PP-V1^R:
1040 plateau potential Renshaw cells. AP: action potential. Threshold values represent the averaged
1041 action potential threshold for single spiking V1^R and repetitive spiking V1^R and the averaged
1042 plateau potential threshold for plateau potential V1^R. Peak amplitude values represent the
1043 averaged peak amplitude of the action potential for single spiking V1^R, the averaged peak
1044 amplitude of the first action potential in a train for repetitive spiking V1^R and the averaged
1045 peak amplitude of plateau potentials for plateau potential V1^R. Half width values represent the
1046 averaged half width of the action potential for single spiking V1^R, the averaged half width of
1047 the first action potential in a train for repetitive spiking V1^R and the averaged half width of
1048 plateau potentials for plateau potential V1^R. Rate of rise values represent the averaged rate of
1049 rise of the action potential for single spiking V1^R, the averaged rate of rise of the first action
1050 potential in a train for repetitive spiking V1^R and the averaged rate of rise of plateau potentials
1051 for plateau potential V1^R. Values are expressed as mean \pm SD. Input resistance of SS-V1^R,
1052 input resistance of RS-V1^R and input resistance of PP-V1^R were not significantly different (P
1053 = 0.17).

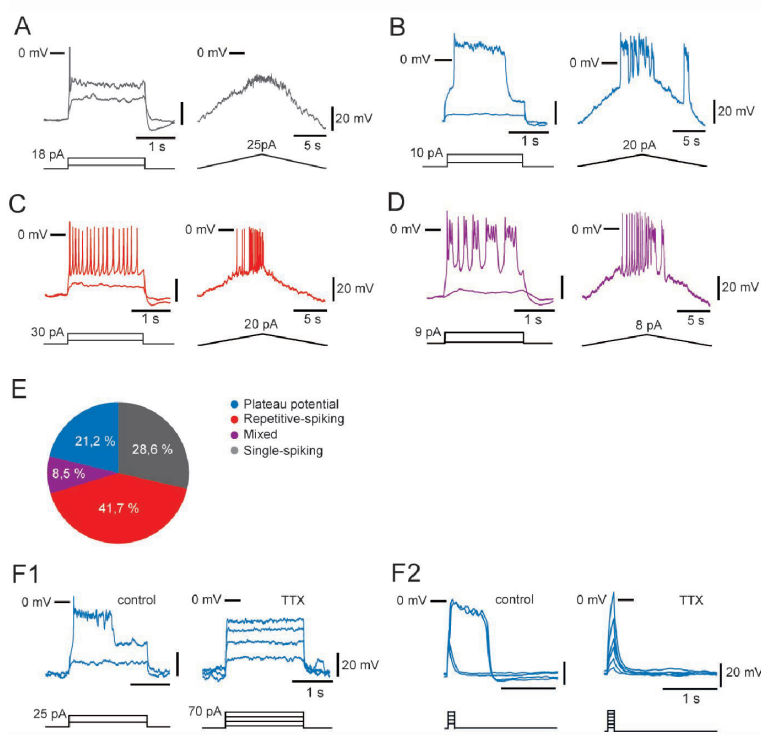


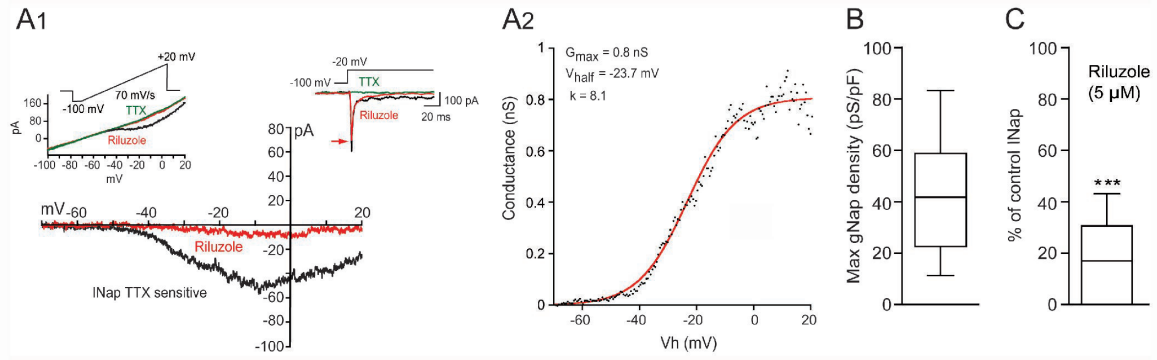


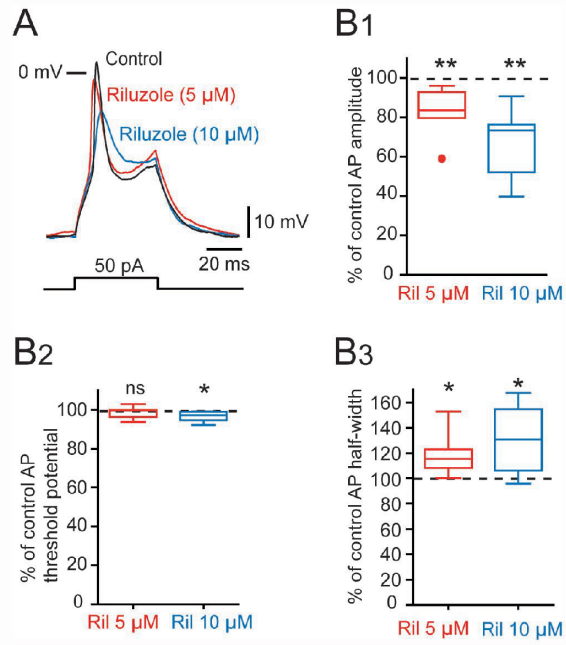


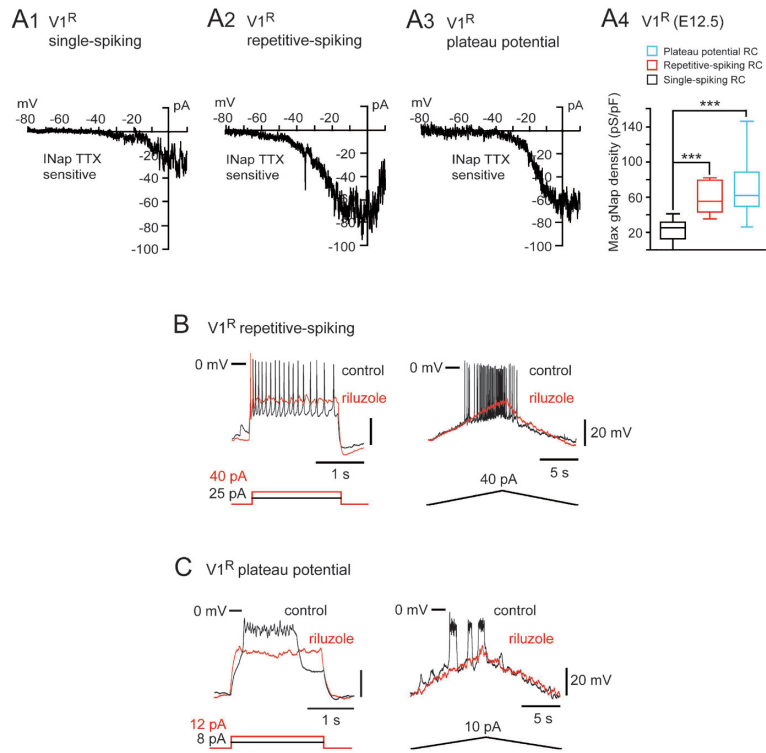












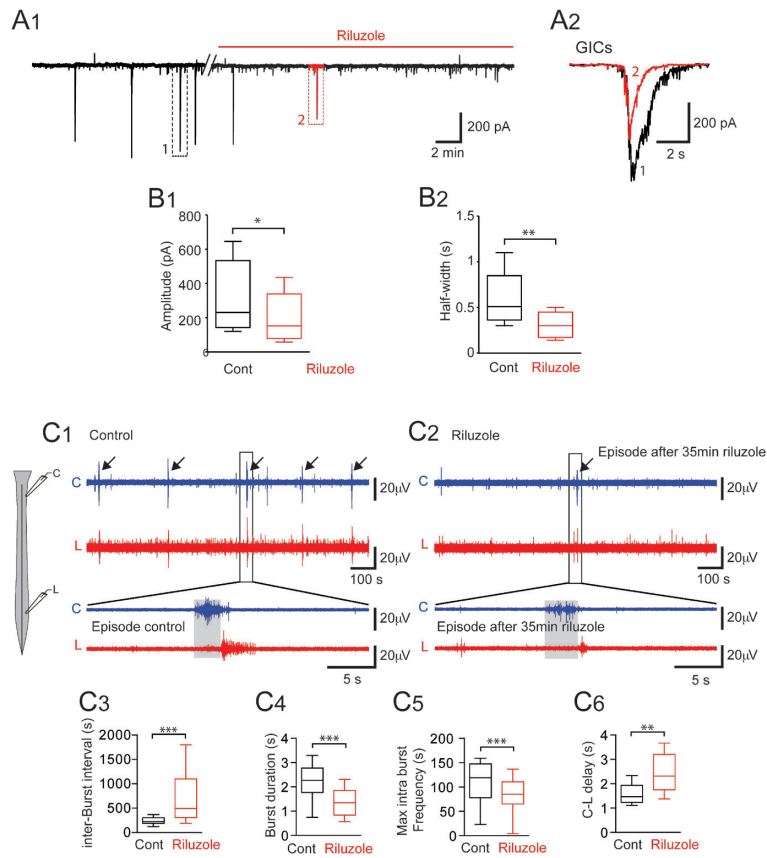


Table 1. Primary antibodies

Primary antibody	Company	Reference	Host/isotype	Dilution
anti-calbindin-D _{28k}	Swant, Switzerland	(Swant Cat# CB38, RRID:AB_2721225)	Rabbit polyclonal	1:1500
anti-FoxD3	provided by C.Birchmeier, MDC Berlin, Germany	Storm R, et al.(2009) Development. ;136:295–305.	Guinea pig polyclonal	1:5000
anti-MafB	Bethyl Laboratories	Bethyl Cat# IHC-00351, RRID:AB_1279487	Rabbit polyclonal	1:1000
anti-GABA	Sigma-Aldrich	Sigma-Aldrich Cat# A0310, RRID:AB_476667	Mouse monoclonal	1:800
Anti-synaptophysin	Synaptic System	Synaptic Systems Cat# 101 011, RRID:AB_887824	Mouse monoclonal	1:1500
Anti-GFP	Aves Labs	Aves Labs Cat# GFP-1020, RRID:AB_10000240)	Chicken polyclonal	1 :1000

	Single-spiking V1 ^R (SS)	Repetitive- spiking V1 ^R (RS)	Plateau potential V1 ^R (PP)
Whole cell capacitance (pF)	13.3 ± 2.8 N = 82	15.3 ± 4.5 N = 60	12.4 ± 3.6 N = 50
Input resistance (MOhm)	1298 ± 682 N = 82	1156 ± 616 N = 60	1254 ± 508 N = 50
Threshold (mV)	-34.1 ± 3.3 N = 46	-33.6 ± 4.9 N = 53	-35.9 ± 6.0 N = 36
peak amplitude (mV)	-6.8 ± 6.1 N = 46	3.2 ± 6.7 N = 53	3.4 ± 10.3 N = 36
half width (ms)	11.2 ± 8.2 N = 46	12.8 ± 6.9 N = 53	705.7 ± 631.7 N = 36
rate of rise (mV/ms)	8.4 ± 3.8 N = 27	13.4 ± 9.4 N = 27	6.2 ± 3.7 N = 19

Table 2: Intrinsic functional properties of V1^R.

SS-V1^R: single-spiking Renshaw cells, RS-V1^R: repetitive-spiking Renshaw cells, PP-V1^R: plateau potential Renshaw cells. AP: action potential. Threshold values represent the averaged action potential threshold for single spiking V1^R and repetitive spiking V1^R and the averaged plateau potential threshold for plateau potential V1^R. Peak amplitude values represent the averaged peak amplitude of the action potential for single spiking V1^R, the averaged peak amplitude of the first action potential in a train for repetitive spiking V1^R and the averaged peak amplitude of plateau potentials for plateau potential V1^R. Half width values represent the averaged half width of the action potential for single spiking V1^R, the averaged half width of the first action potential in a train for repetitive spiking V1^R and the averaged half width of plateau potentials for plateau potential V1^R. Rate of rise values represent the averaged rate of

rise of the action potential for single spiking $V1^R$, the averaged rate of rise of the first action potential in a train for repetitive spiking $V1^R$ and the averaged rate of rise of plateau potentials for plateau potential $V1^R$. Values are expressed as mean \pm SD. Input resistance of SS- $V1^R$, input resistance of RS- $V1^R$ and input resistance of PP- $V1^R$ were not significantly different ($P = 0.17$).